PFC/RR-87-22 DOE/ET-51013-244

Reconstruction Of Vacuum Flux Surfaces From Diagnostic Measurements In A Tokamak

Hakkarainen, S.P.; Freidberg, J.P.

December 1987

Plasma Fusion Center
Massachusetts Institute of Technology
Cambridge, Massachusetts 02139 USA

RECONSTRUCTION OF VACUUM FLUX SURFACES FROM DIAGNOSTIC MEASUREMENTS IN A TOKAMAK

S. P. Hakkarainen
J. P. Freidberg

MIT Plasma Fusion Center
167 Albany Street
Cambridge MA 02139

December 2nd, 1987

Abstract

The shape of a tokamak plasma is determined from measurements of the magnetic flux and one component of the poloidal magnetic field at the vacuum chamber wall. The problem is solved by an application of the Vector Green's theorem for the poloidal flux function, allowing a formulation which overcomes the inherent ill–posedness of the problem while maintaining the computational speed necessary for between shot analysis. The expansion functions are one–dimensional Fourier Transforms in a poloidal-angle-like variable along the direction of the wall. An error analysis is presented that shows the existence of an optimal number of terms in the Fourier sum to maximize the accuracy of the solution. It is also shown that even with random measurement errors, the solution has the same accuracy as the input data from the diagnostic measurements, at least if the maximum error is less than 5%.

I Introduction

A. Experimental Problem

Magnetic diagnostic techniques have developed rapidly in recent years in conjunction with the need to analyze sophisticated plasma fusion experiments. One area of interest involves the diagnosing of strongly non-circular plasmas, perhaps including a divertor generated separatrix. A corresponding classic problem facing the experimentalist is that of determining the shape of the plasma boundary, given an appropriate set of externally measured magnetic probe data.

This problem is ill-posed mathematically, and herein lies the difficulty. Specifically, the aim of the problem is to determine the shape of the flux surfaces $\psi(R,Z) = \text{const.}$ where the flux function satisfies the vacuum form of the Grad-Shafranov equation[1],

$$\Delta^* \psi = 0 \tag{1}$$

$$\Delta^* \psi \equiv R^2 \nabla \cdot (\nabla \psi / R^2) \tag{2}$$

The boundary conditions assume that ψ and its normal derivative $\mathbf{n} \cdot \nabla \psi$ (i.e. tangential magnetic field) are specified on a known surface exterior to the plasma. This is an accurate approximation to the experimental situation in which tangential magnetic field probes and flux loops are located on the vacuum chamber. Since the operator Δ^* is elliptic, the mathematical problem of interest requires the solution of an elliptic partial differential equation, subject to Cauchy boundary-conditions. As is well known this is an ill-posed problem. In principle, small changes in the boundary data lead to large changes in the solution a short distance away, a mathematically unstable situation.

B. Existing Mathematical Procedures

The Cauchy problem for elliptic equations has been extensively studied and is relatively well understood[2]. A number of practical methods have been devised to overcome the ill-posedness. These methods are usually based on an expansion of the flux function in terms of solutions to the vacuum Grad-Shafranov equation; that is

$$\psi(R,Z) = \sum c_i \chi_i(R,Z) \tag{3}$$

with the basis functions χ_i satisfying

$$\Delta^* \chi_i = 0. \tag{4}$$

Stabilising functionals are also often employed in the procedure for inverting or quasi–inverting (minimisation in the least squares sense of some cost function involving the measurement data) the Grad–Shafranov operator.

One class of solution procedures makes use of an expansion for ψ in terms of orthogonal toroidal functions. Such procedures were used for the Tuman-3 tokamak[3] and the ISX-B[4] experiment. In these cases, no information about the plasma current distribution is required. The coefficients c_i are determined to directly give a best fit to both ψ and $\mathbf{n}\cdot\nabla\psi$ on the boundary. One then uses the general radial and angular dependence of the expansion functions to determine ψ away from the boundary. This procedure works reasonably well in practice, although it suffers from several drawbacks. The main difficulty is that the procedure is quite sensitive to the ill-posedness, as no information is provided about the plasma current. The situation is particularly difficult because the expansion functions are in general not natural to the probe geometry, thus implying the need for many terms in the expansion. As will shown below, the errors associated with ill-posedness increase rapidly with the number of expansion functions.

Another class of solution procedures eliminates the ill-posedness by assuming a certain model for the plasma current, *viz.* a filament model. Such a procedure was first proposed by Wootton[5], who makes use of an expansion in the inverse aspect ratio in his analysis. A general procedure where the filament current magnitudes were obtained by minimising

a least squares type cost function assuming fixed locations for the filaments was used in ISX-B[6]. Stabilising functionals were used in determining the plasma shape for Doublet III[7] while the filament model for the plasma was retained. Methods of this type work reasonably well in practice but still suffer from two drawbacks. First, the weight factors employed in the stabilising functionals seem arbitrary, an important point since the results obtained depend quite strongly on the particular weight factor used. Second, for high accuracy, a good approximation is required for the plasma current distribution. This is a difficult task unless one is willing to solve the full Grad-Shafranov equation, a costly procedure in terms of computer time for between shot analysis. Note that in principle the shape of the plasma is completely determined by the boundary data, and no information about the plasma current distribution is required. The purpose of introducing the plasma properties is solely to overcome the ill-posedness.

A procedure based on using a current sheet on a control surface to represent the plasma current is now routinely used at JET[8]. Here again, ψ is expanded in terms of two–dimensional basis functions and the observed fields are matched with the calculated ones in the least squares sense. A good overview of all the existing methods has been given by Braams[9].

C. New Procedure

We have developed a fast [270 ms CPU on a DEC VAX–780] and accurate method to solve for the poloidal flux function in the vacuum region. The method requires no knowledge of the plasma current distribution. The inherent ill-posedness of the problem is overcome by a formulation based on a non-standard application of Green's theorem. Our results show that in realistic practical applications the accuracy of the calculated solution on the plasma surface is approximately the same as the accuracy of the input data on the measurement surface.

The procedure assumes that ψ and $\mathbf{n} \cdot \nabla\psi$ are specified on a given surface exterior to the plasma, e.g. the vacuum chamber. The Green's function formulation allows us to calculate the angular dependence of ψ and $\mathbf{n} \cdot \nabla\psi$ on a sequence of conveniently chosen surfaces filling the region interior to the measurement surface. The advantages of this

procedure are twofold. First, the Green's function method requires no explicit knowledge of the radial dependence of the solution or any associated expansion functions. This is particularly important because the measurement geometry is in general quite complicated, and simple, natural radial expansion functions do not exist. Second, since the solution on each of the interior surfaces involves the determination of the angular dependence of a periodic function, the obvious choice of expansion functions corresponds to a Fourier series. Furthermore, as is shown in the analysis, there is a natural choice for the angle coordinate on the measurement surface and each of the interior surfaces. This ultimately results in the need for relatively few Fourier harmonics to obtain a given accuracy.

The speed of the method (in practice) is due to the fact that all computations related to the Green's functions can be carried out ahead of time once the experimental geometry has been determined, and the results stored on disk. The data storage requirements are quite modest: in addition to the locations of the equilibrium coil currents one needs to typically store 10 complex matrices of size usually no greater than 30×30. The actual computational requirements to solve for ψ are a one dimensional Fourier analysis of the measurement data, approximately 10 matrix multiplications and the one dimensional Fourier reconstruction to obtain the solution in real space, a very rapid procedure indeed.

D. Accuracy

In the practical implementation of the procedure, two steps are taken which greatly enhance the accuracy of the solutions. First, it is assumed that the values of the net plasma current, and the currents in the equilibrium coils, the ohmic transformer, and any other active and passive poloidal field coils are known and can be reasonably well approximated by a sequence of circular current filaments. The flux and tangential magnetic field due to these known current filaments are subtracted from the measurement data prior to the calculation. Once the solution procedure is completed the identical contributions are added back to form the final solution. Note that small errors in the measurements of the coil currents are not important as precisely the same contributions are first subtracted and then added to the solution. The benefit of this step is that once the initial subtraction has been carried out, the resulting input data is a much smoother function; that is, the presence

of large localized coil currents near the measurement probes leads to a high harmonic content in the measurement data. Analytically subtracting these known contributions eliminates most if not all of the high harmonic content. This is a critical point, since, as discussed below, the basic ill-posedness of the problem increases considerably as the number of harmonics is increased.

The second step improving accuracy is the recognition that there is an optimum number of harmonics (typically 4–5 for our application) that should be maintained in the analysis. Specifically, even if the number of measurement probes is increased by a large factor, indicating high harmonic accuracy in the input data, one should still carry out the procedure with a much lower, "optimum" number of harmonics to obtain the most accurate ψ. The existence of an optimum is the result of the competition between poor resolution with too few harmonics versus poor accuracy due to ill-posedness with too many harmonics. The relationship between ill-posedness and harmonic content can be investigated through a simple example.

Consider a right circular cylinder of radius $r = a$ and the function ϕ satisfying Laplaces equation within the cylinder:

$$\nabla^2 \phi = 0 \tag{5}$$

In analogy with the diagnostic problem assume the boundary conditions are given by

$$\begin{aligned} \phi(a,\theta) &= (\phi_m + \epsilon\phi_1)\cos m\theta \\ \frac{\partial \phi}{\partial r}(a,\theta) &= \frac{m}{a}(\phi_m - \epsilon\phi_1)\cos m\theta \end{aligned} \tag{6}$$

Here, ϕ_m is the correct amplitude of the m'th harmonic and $\epsilon\phi_1$ is the error, perhaps due to detector accuracy or calibration procedures. The error amplitude $\epsilon\phi_1$ is assumed independent of m and is scaled as the product of the small number ϵ with the fundamental $m = 1$ harmonic amplitude ϕ_1. This is a good approximation to the error situation in an actual experiment. When $\epsilon = 0$, the solution is

$$\phi = \phi_m \left(\frac{r}{a}\right)^m \cos m\theta \tag{7}$$

which is well behaved and regular for $0 < r < a$. For ϵ small but non-zero the solution inside the cylinder becomes

$$\phi = \phi_m \left(\frac{r}{a}\right)^m \cos m\theta + \epsilon\phi_1 \left(\frac{a}{r}\right)^m \cos m\theta \tag{8}$$

If the "plasma surface" corresponds to some interior surface $r = r_0 < a$, then the ratio of the error in the "calculated" solution [Eq. (8)] to the "exact" solution [Eq. (7)] on the surface $r = r_0$ is given by

$$\frac{\phi(\text{error})}{\phi(\text{exact})} = \epsilon \left(\frac{\phi_1}{\phi_m}\right) \left(\frac{a}{r_0}\right)^{2m} \tag{9}$$

The quantity ϕ_1/ϕ_m is in general an increasing function of m for large m. Hence, the error in the solution increases at least exponentially with harmonic number m for fixed ϵ and (r_0/a). It is for this reason that it is important for the input data be as smooth as possible. The analysis also explains why accuracy degrades when the number of harmonics becomes too large thus implying the existence of an optimum number of harmonics. These points are discussed in detail in Sec. IV.

In summary, the purpose of this study is to provide a reliable formulation of the diagnostic problem, leading to a rapid and accurate determination of the flux function despite the ill-posedness. The nature of the ill-posedness is investigated in detail for realistic experimental situations, allowing a reliable determination of the accuracy of the procedure. A discussion is also presented of an issue of experimental importance viz. how many magnetic field probes and flux loops are required to provide sufficiently accurate input data for a correspondingly accurate determination of the plasma surface.

II Formulation

A. Statement of the Problem

Consider the experimental diagnostic problem that arises in many axisymmetric toroidal fusion devices. Surrounding the plasma is a vacuum chamber upon which is mounted a series of magnetic probes and flux loops which measure the poloidal flux ψ, and the component of poloidal magnetic field tangent to the vacuum chamber, B_t. Experimentally, one would like to use this data to calculate the vacuum flux surfaces, including the location of the separatrix if one is present.

The situation is illustrated in Figure 1. The surface S_1 represents the vacuum chamber upon which ψ and B_t are specified. In general S_1 is not a flux surface because of the short resistive diffusion time of the vacuum chamber.

The region of interest lies between the vacuum chamber and the last flux surface carrying plasma current denoted by ψ_a. In systems with a divertor, ψ_a corresponds to the separatrix, as shown in Figure 1. In systems with a limiter, ψ_a represents the flux surface just intersecting the limiter. A critical point is that the region of interest corresponds to a vacuum region: $\nabla \times \mathbf{B}_p = \nabla \cdot \mathbf{B}_p = 0$ where $\mathbf{B}_p$ is the poloidal magnetic field.

The analysis presented here describes a procedure for calculating ψ and B_t on any arbitrary interior surface, such as S_2, lying in the vacuum region. Once ψ is known, it is then a simple matter to calculate B_n, the magnetic field normal to S_2.

It is important to realize that the procedure can also be used to calculate ψ and B_t on arbitrary surfaces such as S_3 and S_4 that intersect or lie within the last surface carrying current. This follows by recognizing that the plasma current density J_ϕ consistent with the observed ψ and B_t on S_1 is not unique. For example, in a circular cross section plasma, J_ϕ can be replaced by an equivalent set of multipoles on axis, and the field external to plasma remains unchanged. In systems with more general cross sections one can assume that a more complicated, but nonetheless equivalent current density distribution can be found which lies entirely within the last observation surface (S_4 in Figure 1). We emphasize that it is not necessary to explicitly calculate such a J_ϕ, but only to recognize that one exists.

The region between the equivalent J_ϕ and the vacuum chamber is now entirely comprised of vacuum, thus allowing application of the procedure over a wider region of space. Clearly, however, the resulting solutions are valid only in the true vacuum region lying between the vacuum chamber and the surface $\psi = \psi_a$. It is the application of the procedure to such surfaces as S_3 and S_4 that ultimately allows the determination of the flux surface $\psi = \psi_a$.

It should again be noted that the surfaces S_j, $(j \geq 2)$ used in the analysis are arbitrary and are chosen for mathematical convenience. In general they will not be flux surfaces since ψ is not known prior to the calculation. By applying the procedure to a sufficient number of S_j, ψ and $\mathbf{B}_p$ can be determined over the entire region of interest.

The mathematical formulation of the procedure is based on a somewhat non-standard application of the vector Green's theorem. The goal is to derive and then simultaneously solve a set of coupled integral equations for ψ and $\mathbf{n} \cdot \nabla\psi$ in the vacuum region.

The analysis begins with the specification of the poloidal magnetic field which in an axisymmetric toroidal geometry can be written as

$$\mathbf{B}_p = \frac{\nabla\psi \times \mathbf{e}_\phi}{R} \tag{10}$$

Here ψ is the unknown flux function to be determined and (R, ϕ, Z) are standard cylindrical coordinates. (See Figure 1.) Since the region of interest is a vacuum, ψ must satisfy

$$\Delta^*\psi \equiv R^2\nabla \cdot \left(\nabla\psi/R^2\right) = 0 \tag{11}$$

The boundary conditions are chosen to represent the experimental situation: the poloidal flux and tangential field are specified on the surface S_1. In terms of ψ this is equivalent to

$$\psi\Big|_{S_1} = \psi_b \tag{12a}$$

$$\frac{\mathbf{n} \cdot \nabla\psi}{R}\Big|_{S_1} = B_t \tag{12b}$$

where $\mathbf{n}$ is the outward normal to S_1 and ψ_b, B_t are given input data which are functions of poloidal angle. The mathematical statement of the problem under consideration is the requirement that Eq. (11) be solved subject to Eq. (12).

Note that Δ^* is an elliptic operator while Eq. (12) corresponds to Cauchy type boundary conditions. As is well known from the theory of partial differential equations, the problem just formulated is ill-conditioned; that is, the correct amount of boundary data is provided, but it is distributed improperly for an elliptic problem. The procedure presented here provides an effective method for solving the ill-conditioned problem by making use of a non-standard application of the vector Green's theorem.

B. Green's Theorem for the Vector Potential

The first step in the procedure is to express the solution of $\Delta^*\psi = 0$ in terms of the vector Green's theorem using the infinite space Green's Function. In applying the theorem, note that the region of interest is the vacuum region bounded by the vacuum chamber S_1 and any arbitrarily chosen interior surface S_2. One starts with the general three dimensional vector Green's theorem for the vector potential $\mathbf{A}$ given by[10](see Appendix A)

$$\sigma\mathbf{A} = \sum_{j=1}^{2} \int_{S_j} \left[(\mathbf{n}' \cdot \mathbf{A}') \nabla' \hat{G} + (\mathbf{n}' \times \mathbf{A}') \times \nabla' \hat{G} + \hat{G} (\mathbf{n}' \times \nabla' \times \mathbf{A}') \right] dS' \qquad (13)$$

Here primed coordinates denote integration variables, unprimed variables denote observation point, $\mathbf{n}$ is the outward pointing normal to the integration surface and $\hat{G} = -(1/4\pi)/|\mathbf{r}' - \mathbf{r}|$. The quantity σ depends upon the exact location of the observation point with respect to the region of interest and is given by

$$\sigma = \begin{cases} 1 & (R, Z) \text{ between } (S_1, S_2) \\ 1/2 & (R, Z) \text{ on } S_1 \text{ or } S_2 \\ 0 & (R, Z) \text{ outside } (S_1, S_2) \end{cases} \qquad (14)$$

The next step is to simplify Eq. (13) by making use of the assumption of axisymmetry and the fact that only $A_\phi \equiv \psi/R \neq 0$. A short calculation yields

$$\sigma\psi = \sum_{j=1}^{2} \int_{S_j} \frac{1}{R'^2} \left[\psi' \left(\mathbf{n}' \cdot \nabla' \hat{H} \right) - \hat{H} \left(\mathbf{n}' \cdot \nabla' \psi' \right) \right] dS' \tag{15}$$

where the Green's function for the vector potential has the form

$$\hat{H}\left(R', \phi', Z'; R, \phi, Z\right) = -\frac{R'R}{4\pi} \frac{\cos\left(\phi' - \phi\right)}{|\mathbf{r}' - \mathbf{r}|} \tag{16}$$

and

$$|\mathbf{r}' - \mathbf{r}| = \left[R'^2 + R^2 - 2RR' \cos\left(\phi' - \phi\right) + \left(Z' - Z\right) \right]^{1/2} \tag{17}$$

The two basic equations used in the solution procedure are obtained by applying Eq. (15) to the cases where the observation point first lies on the surface S_2 and then on the surface S_1. This gives

$$\begin{aligned} \frac{1}{2}\psi_2 - \int_{S_2} \frac{1}{R_2'^2} \left[\psi_2' \left(\mathbf{n}_2' \cdot \nabla' \hat{H}_{22} \right) - \hat{H}_{22} \left(\mathbf{n}_2' \cdot \nabla' \psi_2' \right) \right] dS_2' \\ = \int_{S_1} \frac{1}{R_1'^2} \left[\psi_1' \left(\mathbf{n}_1' \cdot \nabla' \hat{H}_{12} \right) - \hat{H}_{12} \left(\mathbf{n}_1' \cdot \nabla' \psi_1' \right) \right] dS_1' \end{aligned} \tag{18}$$

$$\begin{aligned} \frac{1}{2}\psi_1 - \int_{S_1} \frac{1}{R_1'^2} \left[\psi_1' \left(\mathbf{n}_1' \cdot \nabla' \hat{H}_{11} \right) - \hat{H}_{11} \left(\mathbf{n}_1' \cdot \nabla' \psi_1' \right) \right] dS_1' \\ = \int_{S_2} \frac{1}{R_2'^2} \left[\psi_2' \left(\mathbf{n}_2' \cdot \nabla' \hat{H}_{21} \right) - \hat{H}_{21} \left(\mathbf{n}_2' \cdot \nabla' \psi_2' \right) \right] dS_2' \end{aligned} \tag{19}$$

Here, the subscripts refer to the surface under consideration. Equations (18) and (19) should be viewed as two coupled integral equations for the unknowns ψ_2 and $\mathbf{n} \cdot \nabla\psi_2$ in terms of the known boundary data ψ_1 and $\mathbf{n} \cdot \nabla\psi_1$.

III Solution Procedure

Several steps are required to solve the coupled integral equations. First, a coordinate system and surface parametrization must be introduced. Second, these are substituted into the integral equations which then reduce considerably. In particular the explicit ϕ dependence of the Green's function $\hat{H}$ is removed by an analytic integration. Next, the reduced equations are solved by Fourier analysis, resulting in a set of linear algebraic equations in standard form for numerical computation. Finally, several practical experimental and numerical issues are addressed. These steps are discussed below.

A. Coordinate System

The analysis begins with the parametrization of the vacuum chamber surface S_1 and the arbitrary observation surface S_2 in terms of an angle like variable v whose range is $0 < v \leq 2\pi$. Each surface is written as

$$\begin{aligned} R_j &= R_j(v) \\ Z_j &= Z_j(v) \end{aligned} \tag{20}$$

The choice of v is arbitrary. For instance v can represent normalized arclength, or the familiar poloidal angle θ defined by $R_j = R_0 + r_j(\theta)\cos\theta, Z_j = r_j(\theta)\sin\theta$. In Sec. IV it is shown that there exist "natural" choices for v for both the measurement and observation surfaces. For the present analysis, the angle v is treated as arbitrary; the particular choice, based on mathematical and/or numerical convenience, is deferred until the end of the calculation. Since the shape of the vacuum chamber and the observation surface are assumed to be given, $R_j(v), Z_j(v)$ are hereafter considered as known quantities.

The normal vector to each surface can be expressed in terms of R_j and Z_j as follows:

$$\hat{\mathbf{n}}_j(v) = \left(\dot{Z}_j \mathbf{e}_R - \dot{R}_j \mathbf{e}_Z\right)/Q_j \tag{21}$$

where

$$Q_j = \left(\dot{R}_j^2 + \dot{Z}_j^2\right)^{1/2} \tag{22}$$

and $\dot{R}_j$, $\dot{Z}_j$ denote dR_j/dv, dZ_j/dv. Note that the outward normal $\mathbf{n}$ is related to $\hat{\mathbf{n}}$ by : $\mathbf{n}_1 = \hat{\mathbf{n}}_1$ and $\mathbf{n}_2 = -\hat{\mathbf{n}}_2$.

Next, observe that the incremental arc length along each surface can be written as

$$d\ell_j = Q_j dv \tag{23}$$

This implies that the differential area element on each surface has the form

$$dS_j = R_j d\phi d\ell_j = R_j Q_j d\phi dv \tag{24}$$

Finally, it is convenient to introduce the normal derivative as follows

$$Q_j \hat{\mathbf{n}} \cdot \nabla = \dot{Z}_j \frac{\partial}{\partial R_j} - \dot{R}_j \frac{\partial}{\partial Z_j} \equiv \frac{\partial}{\partial n} \tag{25}$$

B. Simplification of the Basic Equations

Upon introducing the coordinate system just discussed, one finds that the basic equations are significantly simplified. The main reduction results from the fact that, because of axisymmetry, the ϕ dependence of the Green's function can be analytically integrated. A short calculations yields

$$\frac{1}{2}\psi_2 + \int_{S_2} \left(\frac{\psi_2'}{R_2'}\frac{\partial H_{22}}{\partial n_2'} - \frac{H_{22}}{R_2'}\frac{\partial \psi_2'}{\partial n_2'}\right) dv' - \int_{S_1} \left(\frac{\psi_1'}{R_1'}\frac{\partial H_{12}}{\partial n_1'} - \frac{H_{12}}{R_1'}\frac{\partial \psi_1'}{\partial n_1'}\right) dv' = 0 \tag{26}$$

$$\frac{1}{2}\psi_1 - \int_{S_1} \left(\frac{\psi_1'}{R_1'}\frac{\partial H_{11}}{\partial n_1'} - \frac{H_{11}}{R_1'}\frac{\partial \psi_1'}{\partial n_1'}\right) dv' + \int_{S_2} \left(\frac{\psi_2'}{R_2'}\frac{\partial H_{21}}{\partial n_2'} - \frac{H_{21}}{R_2'}\frac{\partial \psi_2'}{\partial n_2'}\right) dv' = 0 \tag{27}$$

Here, the reduced Green's function is given by

$$H_{ij} = \int_0^{2\pi} \hat{H}_{ij} d\phi' = -\frac{1}{4\pi} \int_0^{2\pi} \frac{R_i' R_j \cos(\phi' - \phi)\, d\phi'}{|\mathbf{r}_i' - \mathbf{r}_j|} \tag{28}$$

and

$$\left|\mathbf{r}_i' - \mathbf{r}_j\right| = \left[R_i'^2 + R_j^2 - 2R_i'R_j\cos\left(\phi' - \phi\right) + \left(Z_i' - Z_j\right)^2\right]^{1/2} \tag{29}$$

Upon evaluating the integral, one obtains

$$H_{ij} = -\frac{\left(R_i'R_j\right)^{1/2}}{2\pi}\left[\frac{\left(2-k^2\right)K - 2E}{k}\right] \tag{30}$$

where $K(k)$ and $E(k)$ are the complete elliptic functions and

$$k^2 = \frac{4R_i'R_j}{\left(R_i' + R_j\right)^2 + \left(Z_i' - Z_j\right)^2} \tag{31}$$

Also required in the calculation is the normal derivative of H_{ij} which is easily calculated and is given by

$$\frac{1}{R_i'}\frac{\partial H_{ij}}{\partial n_i'} = \frac{1}{2\pi}\left(\frac{R_j}{R_i'}\right)^{1/2}\left\{\Lambda_{ij}\left[\frac{\left(2-k^2\right)E - 2\left(1-k^2\right)K}{k}\right] + \Gamma_{ij}k\left(E-K\right)\right\} \tag{32}$$

with

$$\begin{aligned}\Lambda_{ij} &= \frac{\dot{Z}_i'\left(R_i' - R_j\right) - \dot{R}_i'\left(Z_i' - Z_j\right)}{\left(R_i' - R_j\right)^2 + \left(Z_i' - Z_j\right)^2} \\ \Gamma_{ij} &= \frac{\dot{Z}_i'}{2R_i'}\end{aligned} \tag{33}$$

C. Fourier Analysis

The solution to the basic equations [Eqs. (26) and (27)] can now be found by standard Fourier analysis. The unknowns ψ_2 and $(1/R_2)\,(\partial\psi_2/\partial n_2)$ are expanded on the observation surface S_2 as

$$\psi_2 = \sum_{-L}^{L} a_\ell e^{i\ell v} \tag{34}$$

$$\frac{1}{R_2}\frac{\partial\psi_2}{\partial n_2} = \sum_{-L}^{L} b_\ell e^{i\ell v} \tag{35}$$

In principle the sum over ℓ extends over the range $-\infty < \ell < \infty$. In practice, numerical considerations require that the series be truncated at a finite value $|\ell| = L$. The aim of the Solution Procedure is to calculate the unknown Fourier coefficients a_ℓ, b_ℓ in terms of the input data.

In a similar manner, the input quantities ψ_1 and $(1/R_1)\,(\partial\psi_1/\partial n_1)$ are expanded on the vacuum chamber surface S_1 as

$$\psi_1 = \sum_{-M}^{M} \hat{a}_m e^{imv} \tag{36}$$

$$\frac{1}{R_1}\frac{\partial\psi_1}{\partial n_1} = \sum_{-M}^{M} \hat{b}_m e^{imv} \tag{37}$$

Note that the coefficients $\hat{a}_m$ and $\hat{b}_m$ are known quantities, easily derivable from the input data which consists of: (1) the vacuum chamber surface $R_1\,(v')$, $Z_1\,(v')$; (2) the poloidal flux on S_1, $\psi_b\,(v')$ and (3) the tangential field on S_1, $B_t\,(v')$. Also the input Fourier series is in general truncated using a different number of terms from the output series. To avoid the problems associated with ill-posedness, the usual situation is characterized by $L \leq M$. Substituting into Eq. (12) yields

$$\hat{a}_m = \frac{1}{2\pi}\int_0^{2\pi} \psi_b e^{-imv}\,dv \tag{38}$$

$$\hat{b}_m = \frac{1}{2\pi}\int_0^{2\pi} Q_1 B_t e^{-imv} dv \tag{39}$$

The Fourier analysis is completed by substituting these expansions into Eqs. (26) and (27), leading to a standard problem in linear algebra

$$\overleftrightarrow{\mathbf{W}} \cdot \mathbf{y} = \overleftrightarrow{\mathbf{V}} \cdot \mathbf{x} \tag{40}$$

The terms are defined as follows. The vector $\mathbf{y}$ is of length $4L + 2$ and consists of the output coefficients a_ℓ and b_ℓ:

$$\mathbf{y} = \begin{pmatrix} \mathbf{a} \\ \cdots \\ \mathbf{b} \end{pmatrix} \tag{41}$$

The vector $\mathbf{x}$ is of length $2M + 2$ and consists of the input coefficients $\hat{a}_\ell$ and $\hat{b}_\ell$:

$$\mathbf{x} = \begin{pmatrix} \hat{\mathbf{a}} \\ \cdots \\ \hat{\mathbf{b}} \end{pmatrix} \tag{42}$$

The matrix $\overleftrightarrow{\mathbf{W}}$ has dimensions $(4L+2) \times (4L+2)$ and can be written as

$$\overleftrightarrow{\mathbf{W}} = \begin{pmatrix} \overleftrightarrow{\mathbf{I}} + \overleftrightarrow{\mathbf{A}} & \vdots & -\overleftrightarrow{\mathbf{C}} \\ \cdots\cdots\cdots\cdots & & \\ -\overleftrightarrow{\mathbf{B}} & \vdots & \overleftrightarrow{\mathbf{D}} \end{pmatrix}, \tag{43}$$

where $\overleftrightarrow{\mathbf{I}}$ is the identity matrix and the elements of $\overleftrightarrow{\mathbf{A}}$, $\overleftrightarrow{\mathbf{B}}$, $\overleftrightarrow{\mathbf{C}}$, and $\overleftrightarrow{\mathbf{D}}$ are given by

$$A_{\ell\ell'} = \frac{1}{\pi}\int_0^{2\pi}\int_0^{2\pi} \left(\frac{1}{R_2'}\frac{\partial H_{22}}{\partial n_2'}\right) e^{i\ell' v' - i\ell v} dv dv' \tag{44}$$

$$B_{\ell\ell'} = \frac{1}{\pi}\int_0^{2\pi}\int_0^{2\pi} \left(\frac{1}{R_2'}\frac{\partial H_{21}}{\partial n_2'}\right) e^{i\ell' v' - i\ell v} dv dv' \tag{45}$$

$$C_{\ell\ell'} = \frac{1}{\pi}\int_0^{2\pi}\int_0^{2\pi} H_{22} e^{i\ell' v' - i\ell v} dv dv' \tag{46}$$

$$D_{\ell\ell'} = \frac{1}{\pi}\int_0^{2\pi}\int_0^{2\pi} H_{21} e^{i\ell' v' - i\ell v} dv dv' \tag{47}$$

The ranges of ℓ and ℓ' are $-L \leq \ell \leq L$ and $-L \leq \ell' \leq L$.

The matrix $\overleftrightarrow{\mathbf{V}}$ has dimensions $(4L+2) \times (4M+2)$ and has the form

$$\overleftrightarrow{\mathbf{V}} = \begin{pmatrix} \overleftrightarrow{\mathbf{P}} & \vdots & -\overleftrightarrow{\mathbf{T}} \\ \cdots\cdots & \cdots & \cdots\cdots \\ \overleftrightarrow{\mathbf{I}} - \overleftrightarrow{\mathbf{S}} & \vdots & \overleftrightarrow{\mathbf{U}} \end{pmatrix} \tag{48}$$

The elements of $\overleftrightarrow{\mathbf{P}}$, $\overleftrightarrow{\mathbf{S}}$, $\overleftrightarrow{\mathbf{T}}$ and $\overleftrightarrow{\mathbf{U}}$ are given by

$$P_{\ell m} = \frac{1}{\pi} \int_0^{2\pi} \int_0^{2\pi} \left(\frac{1}{R_1'} \frac{\partial H_{12}}{\partial n_1'} \right) e^{imv' - i\ell v} dv dv' \tag{49}$$

$$S_{\ell m} = \frac{1}{\pi} \int_0^{2\pi} \int_0^{2\pi} \left(\frac{1}{R_1'} \frac{\partial H_{11}}{\partial n_1'} \right) e^{imv' - i\ell v} dv dv' \tag{50}$$

$$T_{\ell m} = \frac{1}{\pi} \int_0^{2\pi} \int_0^{2\pi} H_{12} e^{imv' - i\ell v} dv dv' \tag{51}$$

$$U_{\ell m} = \frac{1}{\pi} \int_0^{2\pi} \int_0^{2\pi} H_{11} e^{imv' - i\ell v} dv dv' \tag{52}$$

The ranges of ℓ and m are $-L \leq \ell \leq L$ and $-M \leq m \leq M$.

The output vector $\mathbf{y}$ is easily found numerically from Eq. (40) as follows.

$$\begin{aligned} \mathbf{y} &= \overleftrightarrow{\mathbf{M}} \cdot \mathbf{x} \\ \overleftrightarrow{\mathbf{M}} &= (\overleftrightarrow{\mathbf{W}})^{-1} \cdot \overleftrightarrow{\mathbf{V}} \end{aligned} \tag{53}$$

Observe that the elements of $\overleftrightarrow{\mathbf{W}}$ and $\overleftrightarrow{\mathbf{V}}$ depend only upon the shape of the vacuum chamber surface S_1 and the observation surface S_2. Hence, for a given experimental application in which a vacuum chamber and a sequence of N_S observation surfaces are specified, the matrix $\overleftrightarrow{\mathbf{M}}$ need only be computed one time (for each of the N_S surfaces) and stored. Analysis of a given set of probe data then requires the evaluation of two one dimensional Fourier series for $\hat{a}_m$ and $\hat{b}_m$ and N_S matrix multiplications. Typically $N_S \simeq 10$ and the

dimensions of a given matrix $\overleftrightarrow{\mathbf{M}}$ are of the order (30×30). The implication is that the numerical procedure should be very fast indeed.

The implementation of the Solution Procedure is largely a straightforward numerical problem. Still, there are several numerical subtleties and these, along with a concise summary of the relevant relations are given in Sec. III.E and F. Before proceeding however, we present an important practical generalization of the procedure in Sec. III.D.

D. Generalization when ψ and B_t are Measured on Different Surfaces

In many practical situations the poloidal flux ψ, and the tangential magnetic field B_t are not measured at the same poloidal angle or on the same surface. For example, in a typical application the flux probes are located outside the vacuum chamber while the magnetic field probes are on the inside. A further complication is that the vacuum chamber often carries significant currents, particularly during startup. These issues are addressed here and result in straightforward extensions to the Solution Procedure.

The situation of interest is illustrated in Figure 2a. The vacuum chamber has a finite thickness c. B_t and ψ_b are assumed measured on the inner and outer surfaces S_1 and S_0 respectively. The goal of the analysis is to obtain an analytic solution for ψ in the region lying between S_0 and S_1. In particular, once ψ is known on S_1, the problem reduces to one in which the Solution Procedure can be directly applied.

To obtain analytic solutions, two important assumptions are made. First, the distance c between the surfaces S_0 and S_1 is assumed small compared to the average minor radius b of the vacuum chamber: $c \ll b$. This essentially reduces the analysis to a local 1-D problem. Second, the quantities B_t and ψ_b are assumed to change slowly in time with respect to the magnetic diffusion time of the vacuum chamber. This allows a simple expansion solution for the diffusion equation.

The solution for ψ is obtained as follows. The flux function within the vacuum chamber wall satisfies $\Delta^*\psi = -\mu_0 R J_\phi$. In the limit $c \ll b$, then $\Delta^* \approx \partial^2/\partial\rho^2$ where ρ is physical distance measured perpendicular to the vacuum chamber. The origin is chosen such that the surface S_1 corresponds to $\rho = 0$, while S_0 corresponds to $\rho = c$. Consequently, ψ

satisfies

$$\frac{\partial^2 \psi}{\partial \rho^2} \approx -\mu_0 R J_\phi \tag{54}$$

The quantity J_ϕ is found from Faraday's law using the relations $\mathbf{E} = \eta \mathbf{J}$ and $\mathbf{B} = \nabla \times (\psi \mathbf{e}_\phi / R)$ where η is the resistivity of the wall. A simple calculation gives

$$R J_\phi = -\frac{1}{\eta} \frac{\partial \psi}{\partial t} \tag{55}$$

In deriving Eq. (55), a free integration function has been set to zero, corresponding to the requirement that J_ϕ be non-zero only if the flux is changing: that is, there is no externally driven current in the vacuum chamber.

Combining Eqs. (54) and (55) yields the familiar diffusion equation

$$\frac{\partial \psi}{\partial t} = \frac{\eta}{\mu_0} \frac{\partial^2 \psi}{\partial \rho^2} \tag{56}$$

The boundary conditions require

$$\psi(c, v, t) = \psi_b(v, t) \tag{57}$$

$$\frac{\partial \psi}{\partial \rho}(0, v, t) = R_1(v) B_t(v, t) \tag{58}$$

where $\mathbf{n} \cdot \nabla \psi \approx \partial \psi / \partial \rho$.

If ψ_b and B_t vary slowly in time, initial transients occurring during a wall diffusion time can be ignored. (The wall diffusion time is given by $\tau_W \equiv \mu_0 c^2 / \eta$.) The solution for ψ is then obtained by expanding

$$\psi(\rho, v, t) = \psi_b(v, t) + \psi_1(\rho, v, t) + \cdots \tag{59}$$

with $\psi_1 \ll \psi_b$. The flux ψ_1 satisfies

$$\frac{\partial^2 \psi_1}{\partial \rho^2} = \frac{\mu_0}{\eta} \frac{\partial \psi_b}{\partial t}$$

$$\psi_1(c,v,t) = 0 \tag{60}$$
$$\frac{\partial \psi_1}{\partial \rho}(0,v,t) = R_1 B_t$$

The solution for ψ is easily found and is given by

$$\psi = \psi_b - \frac{\mu_0 (c^2 - \rho^2)}{2\eta} \frac{\partial \psi_b}{\partial t} - R_1 B_t (c - \rho) \tag{61}$$

The first correction term represents the effect of current diffusion in the wall while the second correction term represents the small change in flux from $\rho = c$ to $\rho = 0$ because of the finite wall thickness.

From Eq. (61) it follows that ψ and $\mathbf{n} \cdot \nabla \psi$ on the inner surface $\rho = 0$ are given by

$$\mathbf{n} \cdot \nabla \psi \Big|_{S_1} = R_1 B_t \tag{62}$$

$$\psi \Big|_{S_1} = \psi_b - \frac{\mu_0 c^2}{2\eta} \frac{\partial \psi_b}{\partial t} - R_1 B_t c \tag{63}$$

Equations (62) and (63) represent an equivalent set of boundary conditions on S_1 permitting a direct application of the Solution Procedure. The only difference is that $\psi(S_1)$ appearing in Eq. (12a) should be replaced by the more complete form given by Eq. (63).

As a practical matter, when $c/b \ll 1$, the corrections to the boundary conditions due to the chamber thickness c, and the wall diffusion current J_ϕ are each of the order c/b. Even so, it is important to include these corrections because small errors in the input can lead to large errors in the output, a consequence of the ill-posedness.

The last issue to be addressed involves the situation in which the ψ and B_t probes are located at different poloidal angles as shown in Figure 2b. A mathematical representation of the problem is illustrated in Figure 3a. Shown here are curves of R_1 and Z_1 as a function of v. Also shown are the locations of the non-overlapping flux loops and magnetic field probes.

The issue is easily resolved by introducing two separate parametrizations of $R_1(v)$ and $Z_1(v)$ on S_1, one for ψ and the other for B_t. As a specific example, assume that an

equally spaced grid in the angle v is defined consisting of N_p points where N_p represents the number of B_t probes. For simplicity assume there are also N_p flux loops. On the surface $S_{1\psi}$, $R_{1\psi}(v_n)$ and $Z_{1\psi}(v_n)$ are chosen to correspond to the location of the flux loops. Similarly on the surface S_{1B}, $R_{1B}(v_n)$ and $Z_{1B}(v_n)$ represent the location of the B_t probes. The surfaces $R_{1\psi}$, $Z_{1\psi}$, R_{1B}, Z_{1B} are plotted vs v in Figure 3b. Observe that even though the ψ and B_t probes are located on the same physical surface S_1, they appear on different surfaces in v-space.

The net result is that when evaluating $\hat{a}_m$, $\hat{b}_m$ from Eqs. (38)–(39), and $P_{\ell m}$, $S_{\ell m}$, $T_{\ell m}$, $U_{\ell m}$ from Eqs. (49)–(52), one must use the appropriate representation of S_1 (i.e. $S_{1\psi}$ or S_{1B}).

E. Numerical Issues

As stated previously, the implementation of the Solution Procedure is a relatively straightforward numerical problem. There are, however, several subtleties worth discussing involving (1) the consequences of symmetry, (2) the choice of natural angular coordinates, (3) the existence of logarithmic singularities in certain Green's functions, and (4) the subtraction of the external coil currents from the Solution Procedure.

Consider first the effects of symmetry. If the experiment of interest has the flux loops, magnetic probes and trial surfaces possessing up-down symmetry then all of the matrices are purely real: $\overleftrightarrow{\mathbf{A}}$, $\overleftrightarrow{\mathbf{B}}$, $\overleftrightarrow{\mathbf{C}}$, $\overleftrightarrow{\mathbf{D}}$, $\overleftrightarrow{\mathbf{P}}$, $\overleftrightarrow{\mathbf{S}}$, $\overleftrightarrow{\mathbf{T}}$ and $\overleftrightarrow{\mathbf{U}}$. This is true even when the plasma itself does not possess such symmetry, as for instance in a system with a single null poloidal divertor. On the other hand, the input Fourier coefficients $\hat{a}_m$ and $\hat{b}_m$ are purely real only if the plasma and corresponding input probe data have up-down symmetry.

The second issue involves the natural choice of the angle v on each surface of interest. Since the numerical procedure makes extensive use of fast Fourier transform techniques, it is convenient for the information to be specified on an equi-spaced mesh in v. Thus, if there are N_g grid points describing each surface of interest, a mesh v is established as follows:

$$v_n = \frac{2\pi n}{N_g} \qquad 0 \leq n \leq N_g - 1. \tag{64}$$

When calculating the Fourier coefficients of the input data, $\hat{a}_n$ and $\hat{b}_n$, we use a similar equi-spaced mesh in v with N_g replaced by N_p, the number of flux probes and magnetic loops, so that

$$\begin{aligned} R_1(v_n) &= \hat{R}_n \\ Z_1(v_n) &= \hat{Z}_n \end{aligned} \tag{65}$$

where $(\hat{R}_n, \hat{Z}_n)$ are the actual coordinates of the n'th probe. Since N_p is usually not very large, good accuracy in evaluating the elements of $\mathbf{W}$ and $\mathbf{V}$ requires $N_g \gg N_p$. We usually arrange the probes on the measurement surface in such a way that the N_p locations lie on a subset of the N_g grid points so as to ensure that the two parametrisations of the measurement surface are numerically identical at the probe locations.

In general, one can also easily find natural coordinates for the interior surfaces, although these depend upon the specific shape of the surfaces. For example, in the application considered here the interior surfaces are chosen as a set of similar ellipses. Consequently, the natural parametrization of the jth interior surface can be written as

$$\begin{aligned} R_j(v_n) &= R_0 + a_j \cos v_n \\ Z_j(v_n) &= b_j \sin v_n \end{aligned} \tag{66}$$

where (a_j, b_j) are the width and height of the surface under consideration.

The third issue concerns the evaluation of $\overleftrightarrow{\mathbf{A}}$, $\overleftrightarrow{\mathbf{C}}$, $\overleftrightarrow{\mathbf{S}}$, and $\overleftrightarrow{\mathbf{U}}$, the matrices in which the observation surface coincides with the integration surface. Each of the corresponding Green's functions possesses an integrable logarithmic singularity when $v' = v$. While this represents acceptable analytic behavior it leads to problems of numerical accuracy. This

practical difficulty is avoided by adding and subtracting an appropriate function to each Green's function, thereby allowing the logarithmic singularity to be integrated analytically. The modified Green's functions are given as follows.

$$\begin{aligned}
\tilde{H}_{11}(v',v) &= H_{11} - \frac{R_1}{4\pi}\ln\sin^2\left(\frac{v'-v}{2}\right) \\
\tilde{H}_{22}(v',v) &= H_{22} - \frac{R_2}{4\pi}\ln\sin^2\left(\frac{v'-v}{2}\right) \\
\frac{1}{R_1'}\frac{\partial\tilde{H}_{11}}{\partial n_1'}(v',v) &= \frac{1}{R_1'}\frac{\partial H_{11}}{\partial n_1'} - \frac{\dot{Z}_1}{8\pi R_1}\ln\sin^2\left(\frac{v'-v}{2}\right) \\
\frac{1}{R_2'}\frac{\partial\tilde{H}_{22}}{\partial n_2'}(v',v) &= \frac{1}{R_2'}\frac{\partial H_{22}}{\partial n_2'} - \frac{\dot{Z}_2}{8\pi R_2}\ln\sin^2\left(\frac{v'-v}{2}\right)
\end{aligned} \tag{67}$$

When the observation and integration points coincide (i.e. $v' = v$) the logarithmic singularities cancel and each of the modified Green's functions remains finite:

$$\begin{aligned}
\tilde{H}_{11}(v,v) &= \frac{R_1}{4\pi}\left(\ln\frac{\dot{R}_1^2+\dot{Z}_1^2}{16R_1^2}+4\right) \\
\tilde{H}_{22}(v,v) &= \frac{R_2}{4\pi}\left(\ln\frac{\dot{R}_2^2+\dot{Z}_2^2}{16R_2^2}+4\right) \\
\frac{1}{R_1'}\frac{\partial\tilde{H}_{11}}{\partial n_1'}(v,v) &= \frac{1}{4\pi}\left[\frac{\dot{R}_1\ddot{Z}_1-\dot{Z}_1\ddot{R}_1}{\dot{R}_1^2+\dot{Z}_1^2}+\frac{\dot{Z}_1}{2R_1}\left(2+\ln\frac{\dot{R}_1^2+\dot{Z}_1^2}{16R_1^2}\right)\right] \\
\frac{1}{R_2'}\frac{\partial\tilde{H}_{22}}{\partial n_2'}(v,v) &= \frac{1}{4\pi}\left[\frac{\dot{R}_2\ddot{Z}_2-\dot{Z}_2\ddot{R}_2}{\dot{R}_2^2+\dot{Z}_2^2}+\frac{\dot{Z}_2}{2R_2}\left(2+\ln\frac{\dot{R}_2^2+\dot{Z}_2^2}{16R_2^2}\right)\right]
\end{aligned} \tag{68}$$

Using these relations, the matrices $\overleftrightarrow{\mathbf{A}}$, $\overleftrightarrow{\mathbf{C}}$, $\overleftrightarrow{\mathbf{S}}$, and $\overleftrightarrow{\mathbf{U}}$ are given by

$$A_{\ell\ell'} = \frac{1}{\pi}\int_0^{2\pi}\int_0^{2\pi}\left(\frac{1}{R_2'}\frac{\partial\tilde{H}_{22}}{\partial n_2'}\right)e^{i\ell' v'-i\ell v}dvdv' + \frac{F_{\ell'}}{2\pi}\int_0^{2\pi}\frac{\dot{Z}_2}{R_2}e^{i(\ell'-\ell)v}dv \tag{69a}$$

$$S_{\ell m} = \frac{1}{\pi}\int_0^{2\pi}\int_0^{2\pi}\left(\frac{1}{R_1'}\frac{\partial \tilde{H}_{11}}{\partial n_1'}\right)e^{imv'-i\ell v}dvdv' + \frac{F_m}{2\pi}\int_0^{2\pi}\frac{\dot{Z}_1}{R_1}e^{i(m-\ell)v}dv \qquad (69b)$$

$$C_{\ell\ell'} = -\frac{\ell'}{\pi}\int_0^{2\pi}\int_0^{2\pi}\tilde{H}_{22}e^{i\ell'v'-i\ell v}dvdv' - \frac{\ell' F_{\ell'}}{\pi}\int_0^{2\pi}R_2 e^{i(\ell'-\ell)v}dv \qquad (69c)$$

$$U_{\ell m} = -\frac{\ell'}{\pi}\int_0^{2\pi}\int_0^{2\pi}\tilde{H}_{11}e^{imv'-i\ell v}dvdv' - \frac{mF_m}{\pi}\int_0^{2\pi}R_1 e^{i(m-\ell)v}dv \qquad (69d)$$

where

$$F_{\ell'} = \frac{1}{4\pi}\int_0^{2\pi}\ln\sin^2\left(\frac{v'-v}{2}\right)e^{i\ell'(v'-v)}dv' = \begin{cases} -\ln 2 & \ell' = 0 \\ -\dfrac{1}{2|\ell'|} & \ell' \neq 0 \end{cases} \qquad (70)$$

In this form the matrices can be evaluated in a straightforward manner. Finally, note that no numerical problems arise in the evaluation of $\overleftrightarrow{\mathbf{B}}$, $\overleftrightarrow{\mathbf{D}}$, $\overleftrightarrow{\mathbf{P}}$ and $\overleftrightarrow{\mathbf{T}}$ since the observation and integration points lie on different surfaces and hence do not overlap.

The fourth and final numerical issue involves the subtraction of the exterior coil currents prior to the application of the Solution Procedure. This task is readily accomplished by writing the total flux $\hat{\psi}$ as follows:

$$\hat{\psi}(R,Z,t) = \psi(R,Z,t) + \sum_j \mu_0 I_j(t)\,\Psi_j(R,Z) \qquad (71)$$

Here

$$\Psi_j(R,Z) = \frac{(RR_j)^{1/2}}{2\pi}\left[\frac{(2-k^2)K(k) - 2E(k)}{k}\right]$$
$$k^2 = \frac{4RR_j}{(R+R_j)^2 + (Z-Z_j)^2} \qquad (72)$$

and (R_j, Z_j) are the coordinates of the j'th filament. The sum over j includes the currents in the exterior equilibrium field coils and the ohmic transformer. It also includes the net plasma current which is assumed located at any arbitrary interior point, for example $R = R_0$, $Z = 0$. If there are current carrying conductors *internal* to the vacuum chamber,

their currents must be included in the sum. For each of these currents, the corresponding $I_j(t)$ is assumed known. Equation (72) indicates that the contribution to the flux from each current is approximated as that due to a thin circular filament located at (R_j, Z_j).

The task of the Solution Procedure is to accurately calculate the residual contribution to the flux, ψ. Since ψ still satisfies $\Delta^*\psi = 0$, all the previous analysis remains valid. The only difference is that the external current contributions must be subtracted from the boundary data. Consequently, if ψ_b and B_t are the experimentally measured data, the appropriate boundary conditions for the Solution Procedure become

$$\begin{aligned}
\mathbf{n}\cdot\nabla\psi\Big|_{S_1} &= R_1 B_t - \sum_j \mu_0 I_j \mathbf{n}\cdot\nabla\Psi_j \\
\psi\Big|_{S_1} &= \psi_b - \frac{\mu_0 c^2}{2\eta}\frac{\partial\psi_b}{\partial t} - R_1 B_t c \\
&\quad - \sum_j \left[\mu_0 I_j \Psi_j - \frac{\mu_0^2 c^2}{2\eta}\frac{dI_j}{dt}\Psi_j - \mu_0 c I_j \mathbf{n}\cdot\nabla\Psi_j\right]
\end{aligned} \tag{73}$$

Clearly, once ψ has been determined, the external coil contributions must be added back to obtain the full solution $\hat{\psi}$.

F. Summary

For convenience a summary is presented of the basic relations required for the solution procedure.

Coupled integral equations:

$$\frac{1}{2}\psi_2 + \int_{S_2}\left(\frac{\psi_2'}{R_2'}\frac{\partial H_{22}}{\partial n_2'} - \frac{H_{22}}{R_2'}\frac{\partial\psi_2'}{\partial n_2'}\right)dv' - \int_{S_1}\left(\frac{\psi_1'}{R_1'}\frac{\partial H_{12}}{\partial n_1'} - \frac{H_{12}}{R_1'}\frac{\partial\psi_1'}{\partial n_1'}\right)dv' = 0 \tag{74}$$

$$\frac{1}{2}\psi_1 - \int_{S_1}\left(\frac{\psi_1'}{R_1'}\frac{\partial H_{11}}{\partial n_1'} - \frac{H_{11}}{R_1'}\frac{\partial\psi_1'}{\partial n_1'}\right)dv' + \int_{S_2}\left(\frac{\psi_2'}{R_2'}\frac{\partial H_{21}}{\partial n_2'} - \frac{H_{21}}{R_2'}\frac{\partial\psi_2'}{\partial n_2'}\right)dv' = 0 \tag{75}$$

Green's Functions:

$$H_{ij} = -\frac{\left(R_i' R_j\right)^{1/2}}{2\pi}\left[\frac{\left(2-k^2\right)K - 2E}{k}\right] \tag{76}$$

$$\frac{1}{R_i'}\frac{\partial H_{ij}}{\partial n_i'} = \frac{1}{2\pi}\left(\frac{R_j}{R_i'}\right)^{1/2}\left\{\Lambda_{ij}\left[\frac{\left(2-k^2\right)E - 2\left(1-k^2\right)K}{k}\right] + \Gamma_{ij}k\left(E-K\right)\right\} \tag{77}$$

$$k^2 = \frac{4R_i' R_j}{\left(R_i' + R_j\right)^2 + \left(Z_i' - Z_j\right)^2} \tag{78}$$

$$\Lambda_{ij} = \frac{\dot{Z}_i'\left(R_i' - R_j\right) - \dot{R}_i'\left(Z_i' - Z_j\right)}{\left(R_i' - R_j\right)^2 + \left(Z_i' - Z_j\right)^2} \tag{79}$$

$$\Gamma_{ij} = \frac{\dot{Z}_i'}{2R_i'}$$

Fourier analysis:

$$\psi_2 = \sum_{-L}^{L} a_\ell e^{i\ell v} \tag{80}$$

$$\frac{1}{R_2}\frac{\partial \psi_2}{\partial n_2} = \sum_{-L}^{L} b_\ell e^{i\ell v} \tag{81}$$

$$\psi_1 = \sum_{-M}^{M} \hat{a}_m e^{imv} \tag{82}$$

$$\frac{1}{R_1}\frac{\partial \psi_1}{\partial n_1} = \sum_{-M}^{M} \hat{b}_m e^{imv} \tag{83}$$

Input Fourier coefficients:

$$\hat{a}_m = \frac{1}{2\pi}\int_0^{2\pi}\left[\psi_b - \frac{\mu_0 c^2}{2\eta}\frac{\partial \psi_b}{\partial t} - R_1 B_t c + \sum_j\left(\mu_0 I_j H_{1j} - \frac{\mu_0^2 c^2}{2\eta}\frac{dI_j}{dt}H_{1j} - \frac{\mu_0 c I_j}{Q_1}\frac{\partial H_{1j}}{\partial n_1}\right)\right] e^{-imv}dv \tag{84}$$

$$\hat{b}_m = \frac{1}{2\pi}\int_0^{2\pi}\left(Q_1 B_t + \sum_j \frac{\mu_0 I_j}{R_1}\frac{\partial H_{1j}}{\partial n_1}\right)e^{-imv}dv \tag{85}$$

Output Fourier coefficients:

$$\begin{pmatrix}\mathbf{a}\\ \cdots \\ \mathbf{b}\end{pmatrix} = \begin{pmatrix}\overleftrightarrow{\mathbf{I}}+\overleftrightarrow{\mathbf{A}} & \vdots & -\overleftrightarrow{\mathbf{C}}\\ \cdots & \cdots & \cdots \\ -\overleftrightarrow{\mathbf{B}} & \vdots & \overleftrightarrow{\mathbf{D}}\end{pmatrix}^{-1}\cdot\begin{pmatrix}\overleftrightarrow{\mathbf{P}} & \vdots & -\overleftrightarrow{\mathbf{T}}\\ \cdots & \cdots & \cdots \\ \overleftrightarrow{\mathbf{I}}-\overleftrightarrow{\mathbf{S}} & \vdots & \overleftrightarrow{\mathbf{U}}\end{pmatrix}\cdot\begin{pmatrix}\hat{\mathbf{a}}\\ \cdots \\ \hat{\mathbf{b}}\end{pmatrix} \tag{86}$$

Matrix elements:

$$B_{\ell\ell'} = \frac{1}{\pi}\int_0^{2\pi}\int_0^{2\pi}\left(\frac{1}{R_2'}\frac{\partial H_{21}}{\partial n_2'}\right)e^{i\ell' v' - i\ell v}dvdv' \tag{87}$$

$$P_{\ell m} = \frac{1}{\pi}\int_0^{2\pi}\int_0^{2\pi}\left(\frac{1}{R_1'}\frac{\partial H_{12}}{\partial n_1'}\right)e^{imv' - i\ell v}dvdv' \tag{88}$$

$$D_{\ell\ell'} = \frac{1}{\pi}\int_0^{2\pi}\int_0^{2\pi} H_{21}e^{i\ell' v' - i\ell v}dvdv' \tag{89}$$

$$T_{\ell m} = \frac{1}{\pi}\int_0^{2\pi}\int_0^{2\pi} H_{12}e^{imv' - i\ell v}dvdv' \tag{90}$$

$$A_{\ell\ell'} = \frac{1}{\pi}\int_0^{2\pi}\int_0^{2\pi}\left(\frac{1}{R_2'}\frac{\partial \tilde{H}_{22}}{\partial n_2'}\right)e^{i\ell' v' - i\ell v}dvdv' + \frac{F_{\ell'}}{2\pi}\int_0^{2\pi}\frac{\dot{Z}_2}{R_2}e^{i(\ell'-\ell)v}dv \tag{91}$$

$$S_{\ell m} = \frac{1}{\pi}\int_0^{2\pi}\int_0^{2\pi}\left(\frac{1}{R_1'}\frac{\partial \tilde{H}_{11}}{\partial n_1'}\right)e^{imv' - i\ell v}dvdv' + \frac{F_m}{2\pi}\int_0^{2\pi}\frac{\dot{Z}_1}{R_1}e^{i(m-\ell)v}dv \tag{92}$$

$$C_{\ell\ell'} = -\frac{\ell'}{\pi}\int_0^{2\pi}\int_0^{2\pi}\tilde{H}_{22}e^{i\ell' v' - i\ell v}dvdv' - \frac{\ell' F_{\ell'}}{\pi}\int_0^{2\pi} R_2 e^{i(\ell'-\ell)v}dv \tag{93}$$

$$U_{\ell m} = -\frac{m}{\pi}\int_0^{2\pi}\int_0^{2\pi}\tilde{H}_{11}e^{imv' - i\ell v}dvdv' - \frac{mF_m}{\pi}\int_0^{2\pi} R_1 e^{i(m-\ell)v}dv \tag{94}$$

and

$$F_{\ell'} = \begin{cases} -\ln 2 & \ell' = 0 \\ -\dfrac{1}{2|\ell'|} & \ell' \neq 0 \end{cases} \tag{95}$$

Modified Green's functions for arbitrary v' and v:

$$\tilde{H}_{11}(v',v) = H_{11} - R_1 f \tag{96}$$

$$\tilde{H}_{22}(v',v) = H_{22} - R_2 f \tag{97}$$

$$\frac{1}{R_1'}\frac{\partial \tilde{H}_{11}}{\partial n_1'}(v',v) = \frac{1}{R_1'}\frac{\partial H_{11}}{\partial n_1'} - \frac{\dot{Z}_1}{2R_1} f \tag{98}$$

$$\frac{1}{R_2'}\frac{\partial \tilde{H}_{22}}{\partial n_2'}(v',v) = \frac{1}{R_2'}\frac{\partial H_{22}}{\partial n_2'} - \frac{\dot{Z}_2}{2R_2} f \tag{99}$$

and

$$f(v',v) = \frac{1}{2\pi}\ln\sin^2\left(\frac{v'-v}{2}\right) \tag{100}$$

Modified Green's functions for $v' = v$:

$$\tilde{H}_{11}(v,v) = \frac{R_1}{4\pi}(g_1 + 4) \tag{101}$$

$$\tilde{H}_{22}(v,v) = \frac{R_2}{4\pi}(g_2 + 4) \tag{102}$$

$$\frac{1}{R_1'}\frac{\partial \tilde{H}_{11}}{\partial n_1'}(v,v) = \frac{1}{4\pi}\left[h_1 + \frac{\dot{Z}_1}{2R_1}(2 + g_1)\right] \tag{103}$$

$$\frac{1}{R_2'}\frac{\partial \tilde{H}_{22}}{\partial n_2'}(v,v) = \frac{1}{4\pi}\left[h_2 + \frac{\dot{Z}_2}{2R_2}(2 + g_2)\right] \tag{104}$$

and

$$g_i(v) = \ln\frac{\dot{R}_i^2 + \dot{Z}_i^2}{16R_i^2} \tag{105}$$

$$h_i(v) = \frac{\dot{R}_i\ddot{Z}_i - \dot{Z}_i\ddot{R}_i}{\dot{R}_i^2 + \dot{Z}_i^2} \tag{106}$$

Full solution on interior surface k:

$$\hat{\psi} = \psi - \sum_j \mu_0 I_j H_{kj} \tag{107}$$

$$B_t = \frac{1}{R_k Q_k} \frac{\partial \psi}{\partial n_k} - \sum_j \frac{\mu_0 I_j}{R_k Q_k} \frac{\partial H_{kj}}{\partial n_k} \tag{108}$$

This completes the formulation of the Solution Procedure.

IV Results and Discussion

A Test Case

A numerical code has been written to test the accuracy of the Green's Function Solution Procedure. Comparisons with analytic large aspect ratio, circular cross–section plasmas and vacuum chambers have been made. In all such comparisons, the agreement between the analytic and the numerically computed flux function is excellent, with the magnitude of maximum local deviation less than 1 part in 10^5.

As a more realistic test, we consider a model that provides an accurate representation of the poloidal field in the Alcator C-Mod experiment, *viz.* a finite aspect ratio ($R_0/a = 3$), elongated ($\kappa = 1.7$) plasma with a separatrix generated by divertor coils. In order to have an analytic model with which to compare, we choose a set of circular current filaments each carrying current I_j to represent the plasma, the equilibrium field coils and the ohmic transformer. The analytic flux and field at any arbitrary point (R_i, Z_i) can then be written as

$$\psi(R_i, Z_i) = -\sum_j \mu_0 I_j H_{ij}, \tag{109}$$

$$B_i(R_i, Z_i) = -\sum_j \frac{\mu_0 I_j}{R_i Q_i} \frac{\partial H_{ij}}{\partial n_i}, \tag{110}$$

where the reduced Green's function H_{ij} is given by equation (30) and the modulus of the Elliptic functions appearing in H_{ij} is

$$k^2 = \frac{4R_i R_j}{(R_i + R_j)^2 + (Z_i - Z_j)^2}, \tag{111}$$

(R_j, Z_j) being the location of the j'th current filament. The current filament geometry and the corresponding analytic flux contours for typical Alcator C-Mod parameters are illustrated in Figure 4. This represents quite a realistic model upon which we shall test the solution procedure[1].

[1] D. Humphreys and S. Wolfe at MIT Plasma Fusion Center helped us obtain the filament model.

B Computational Surfaces and Error Definition

In applying the procedure we must first identify the measurement surface S_1 and the interior surfaces S_k, $k \geq 2$. For simplicity we choose the measurement surface to be an ellipse of elongation $\kappa = 2.255$ approximating the Alcator C-Mod vacuum chamber. An elliptic shape was chosen for numerical convenience, but it does not constitute a critical assumption, since the exact vacuum chamber shape can easily be incorporated. For the interior surfaces we choose a set of 9 ellipses of various elongations and radii filling the "vacuum" region, the innermost one having a surface area 0.241 times that of the measurement surface. The computational geometry is illustrated in Figure 5, superimposed over the current filaments that represent the plasma, the equilibrium field coils and the ohmic transformer.

The angle v used for parametrizing each surface, and the corresponding $[R_j(v), Z_j(v)]$, are chosen in accordance with equation (66). Also, no attempt has been made to improve accuracy by optimizing the spacing of the probes on the measurement surfaces, which are located at equal v intervals as shown in Figure 5.

Consider now the evaluation of the error. Two different definitions are introduced, a local error as a function of the poloidal angle v, and a Root Mean Squared (RMS) error characterizing the average error on each interior surface. Furthermore, separate errors are required for the flux and the tangential magnetic field. The local errors on any given surface are defined as

$$\begin{aligned} \epsilon_\psi(v) &= \frac{2\pi}{R_0\mu_0 I_p}|\psi_n(v) - \psi_a(v)|, \\ \epsilon_B(v) &= \frac{2\pi}{\mu_0 I_p}\left|\frac{1}{R}\frac{\partial\psi_n}{\partial n}(v) - \frac{1}{R}\frac{\partial\psi_a}{\partial n}(v)\right|, \end{aligned} \tag{112}$$

where the subscript n refers to the numerically computed solution and a to the exact analytic result. Note that the errors are normalized to the plasma current I_p, which determines the characteristic size of ψ and B_t. In this sense the magnitudes of ϵ_ψ and ϵ_B provide a reasonable, absolute measure of the accuracy of the solutions.

As a relative measure of the accuracy, it is useful to compare ϵ_ψ and ϵ_B with the errors in the boundary data, $\hat{\epsilon}_\psi$ and $\hat{\epsilon}_B$, which are also defined in accordance with equation (112),

and are calculated using the difference between the "exact" measured boundary data and the recontructed data from the truncated Fourier series. The latter serve as an input to the Solution Procedure. Clearly, one can at best expect $\epsilon_\psi \sim \hat{\epsilon}_\psi$ and $\epsilon_B \sim \hat{\epsilon}_B$. When $\epsilon_\psi \gg \hat{\epsilon}_\psi$ or $\epsilon_B \gg \hat{\epsilon}_B$, we have an indication of the fact that large errors have developed as a result of ill-posedness.

It is also useful to define RMS errors for each surface to facilitate simultaneous comparisons with many different cases. These are defined in the usual manner:

$$< \epsilon_\psi >= \frac{1}{N_g} \left[\sum_{k=1}^{N_g} \epsilon_\psi^2(v_k) \right]^{1/2} , \tag{113}$$

$$< \epsilon_B >= \frac{1}{N_g} \left[\sum_{k=1}^{N_g} \epsilon_B^2(v_k) \right]^{1/2} , \tag{114}$$

where $v_k = 2(k-1)\pi/N_g$ and N_g is the number of grid points.

C Numerical Computation for the Test Case

As a first test of the Solution Procedure we have numerically computed ψ and $\partial\psi/\partial n$ for the analytic model just described. In carrying out the calculation we assume that there are $N_p = 25$ magnetic probes and flux loops on the measurement surface. The number of grid points is taken to be $N_g = 100$. Also, each of the Fourier series appearing in the analysis is truncated to $L = M = 5$ harmonics. The measurement data for $\hat{\psi}$ and $\mathbf{n} \cdot \nabla\hat{\psi}$ on S_1 is taken exactly from the analytic solution. It is also assumed for simplicity that the magnetic probes and flux loops are overlapping so that the thickness of the vacuum chamber vanishes, $c = 0$. For the results presented in this section, all the external currents as well as the net plasma current represented by a filament at $R = R_0$, $Z = 0$ have been initially subtracted from the solution and then added back at the end.

The first quantity of interest is the accuracy of the input data. Illustrated in Figures 6a and 6b are curves of $\psi_a(v)$, $\psi_n(v)$ and $\hat{\epsilon}_\psi(v)$ on S_1. Similar sets of curves for the tangential field at the surface are shown in Figures 6c and 6d. The Fourier series approximation to the input data is quite accurate for $L = M = 5$ harmonics and $N_p = 25$ probes, with the RMS errors for the input data being $< \hat{\epsilon}_\psi >= 0.02\%$ and $< \hat{\epsilon}_B >= 0.2\%$.

Consider now the results of applying the Solution Procedure. Illustrated in Figures 7a and 7b are the flux contours from the numerically computed solution and the analytic solution respectively. To the resolution of the printer, they are identical. A more quantitative comparison between the measurement surface and the computation surfaces is shown in Figure 8, where we have plotted curves of $< \epsilon_\psi >$ and $< \epsilon_B >$ as functions of x_j, which is defined as the ratio between the cross-sectional areas enclosed by the computation surface S_j and the measurement surface S_1:

$$x_j = \frac{A_j}{A_1}. \tag{115}$$

Note that the RMS errors are quite small, comparable to the errors in the input data; there is no degradation in accuracy due to ill-posedness. The accuracy, in fact, increases when moving towards the plasma centre. This is because, typically, fewer harmonics are required to accurately represent the flux and magnetic field near the plasma centre than at the vacuum chamber wall. We conclude, therefore, that in general it is not appropriate to use the same number of harmonics for each computation surface — a smaller number should be used for inner ones than for those close to the measurement surface.

D Effect of Subtracting External Currents

It has been previously stated that the accuracy of the Solution Procedure is significantly increased by first subtracting the contribution to the flux and field from all the known external currents and then performing the calculation on the residual flux function. At the end, one adds back the contributions from the external currents to obtain the full flux function. This point is illustrated in Figures 9–11.

The calculated flux and the corresponding analytic flux are shown in Figure 9, when the contribution from external currents was retained in the expressions for the input data. Computationally, these results are obtained by setting each $I_j = 0$ in equation (73). The case illustrated here was computed using $N_p = 25$ and $L = M = 5$ corresponding to the same resolution in the input data as in the previous section. However, finite differences in the computed and analytic flux contours can now easily be seen, implying considerably increased errors.

The increase in the errors is due to a combination of poor convergence of the Fourier series for the input data and the natural ill-posedness of the problem. Figure 10 demonstrates the poor convergence, where the exact and truncated Fourier series representations of the input data are shown for ψ and $\partial\psi/\partial n$ on surface S_1. The convergence deteriorates because of the influence of the nearby external currents, which add significantly to the high harmonic content in the input data. Furthermore, the accuracy of the truncated Fourier series representation is reduced relative to that of the previous section for the same number of harmonics. Indeed, the RMS errors increase by a factor of 10 to $< \hat{\epsilon}_\psi >= 0.2\%$ and $< \hat{\epsilon}_B >= 3\%$ for the input data.

The effect of the ill-posedness is shown in Figure 11. Illustrated are the RMS errors as functions of computation surface S_j. As expected, the magnitude of the errors is considerably higher when the external currents are not subtracted from the calculation, a result of the poor convergence using the same number of harmonics. The increase in the RMS errors as x_j decreases (*i.e.* moving away from the measument surface S_1) is an indication of errors in the higher harmonics in the input data. This leads to an increasing error away from the measurement surface as a result of ill-posedness.

E Effect of Varying the Number of Probes

Having shown that the Solution Procedure is capable of producing quite accurate answers for the flux function in the vacuum region, we now investigate the effect of increasing the number of probes N_p while holding the number of harmonics $M = L$ constant. In accordance to the results of the previous sections, we subtract the contributions from the known external currents and perform the computation on the residual flux function. Intuitively, we expect the critical parameter to be N_p/M, corresponding to the number of measurements available for resolving the highest harmonic used in the computation. Illustrated in Figure 12a are curves of $< \epsilon_\psi >$ as function of N_p/M for several values of M, the number of harmonics, for a typical computation surface S_j. The maximum value of M used in this study is chosen sufficiently low so that the effects of ill-posedness are not important.

We observe that the accuracy of the solution increases (the error decreases) as the number of harmonics M is increased. This is to be expected before the onset of divergence due to ill–posedness. The interesting feature in Figure 12a is the fact that for all values of M the accuracy of the solution saturates when N_p/M exceeds the value 4. Intuitively, once a sufficient number of measurements is available for resolving the highest harmonic, no additional increases in accuracy result from further increase to N_p/M. From an experimantal point of view, this is an important conclusion: there is no need to increase the number of probes beyond $5M$ where M represents the highest significant harmonic content of the measured data as a function of v with the known external currents subtracted out. For this reason we set $N_p/M = 5$ for the cases studied below.

F Effect of Varying the Number of Harmonics

The formulation of the Solution Procedure has not assumed that the number of harmonics used for the input data M equals the number used for the output functions L. It is then natural to investigate whether $M = L$ is always the best choice, and if not, how the two can be best determined. In order to do this, we carry out the Solution Procedure for different values of L at fixed M and $N_p/M = 5$. The optimal L_o at a given M is then chosen as the one that corresponds to the smallest value of $< \epsilon_\psi >$ for the surface S_j in question. A plot of $< \epsilon_\psi >$ versus L is shown in Figure 12b for surface S_8. Observe the existence of the optimum L_o representing the competition between convergence and ill–posedness.

Consider next the variation of L_o with M for surfaces S_4 and S_8 as shown in Figures 13a and 13b, respectively. It is evident that some saturation in the optimal L_o is observed for surface S_8. This can be attributed to the ill–posedness of the problem as discussed before, and a full analysis to determine the optimal L_o will be given after the next section. The conclusion from this section is that in general the choice $L = M$ appears to give the highest accuracy over almost the entire parameter range of interest. Furthermore, accuracy continues to improve as the value of M is increased. This is a consequence of the fact that the "exact" boundary data from the analytic solution is used as an input to the numerical solution. Numerical noise in the data is so low that modern computers provide accurate answers, even with 15 harmonics present. We shall see in the next section, that

when random errors are deliberately introduced into the measurement data (representing the actual experimental situation), there is an optimum M_o for each surface; values of $L \gtrsim 8$ invariably lead to large errors due to ill-posedness, even when the random errors are relatively small, approximately 1%. Usually it is not necessary to have a value of M larger than the largest value of L.

G Effect of Random Errors in Measurements

As just stated, in order to more effectively simulate a realistic experimental situation, we introduce random errors into the given boundary data. These might correspond to errors in the measured values of the magnetic fields or currents due to uncertainties in the diagnostic equipment, *eg.* orientation of the probes, calibration procedures *etc.* Specifically, we assume that the locations of the equilibrium field coils, the ohmic transformer and the diagnostic probes are accurately known, while the quantities measured during the experiment, the magnetic flux and fields as well as the currents in the plasma and external coils, contain random errors. These are introduced in our model by changing the values of the "measured" flux and field on the boundary S_1 (obtained from the analytic filament model) by a maximum of ε_M so that each measurement, ψ_j say, is changed to $\psi_j(1+\varepsilon_M r_j)$, where r_j is a uniformly distributed random number in the interval $[-1,1]$. Similarly, currents in the equilibrium coils and the ohmic transformer I_j as well as the total plasma current I_p are changed to $I_j(1+\varepsilon_M r_j)$ and $I_p(1+\varepsilon_M r_j)$ respectively. Several values of ε_M have been studied up to $\varepsilon_M = 0.05$. The results given below correspond to the case $\varepsilon_M = 0.01$, although qualitatively, the same conclusions apply to all values of ε_M investigated.

Figures 14a and 14b illustrate the numerically computed and analytic flux countours respectively, when 1% random errors are present in all measurements. The calculation is performed with $N_p = 25$ and $M = L = 3$. The two flux plots are very close to identical. Figure 15a shows the RMS error $< \epsilon_\psi >$ as a function of the measurement surface S_j. It can be seen that for $x_j > 0.4$ the errors in the calculated values are approximately the same as the errors in the input data, which is the best accuracy that we can expect to obtain. For $x_j < 0.4$ the effects of ill-posedness become apparent. Figure 15b shows, for comparison with the boundary values given before, the calculated and analytic flux as a

function of v for the innermost surface in the calculation, S_9. The approximation is seen to be reasonable.

We next investigate the effect of varying L, the number of output harmonics, for given values of M, the number of input harmonics. The optimal L_o is chosen as before to correspond to the smallest values of $< \epsilon_\psi >$ for the given surface. The optimal L_o is shown in Figures 16a and 16b as a function of M for the same two surfaces S_4 and S_8 as in the previous section.

There are several important points to note. First, on a given surface, S_8 say, the optimal L_o equals M for sufficiently small values of $M \leq 3$. For $M \geq 4$, there is a rapid saturation in accuracy. Even with very high resolution of the input data, characterized by $M = 13$, $N_p/M = 5$, the optimal number of output harmonics remains fixed at $L_o = 3$, a dramatic demonstration of the consequences of ill–posedness. Clearly, from an experimental point of view, the optimal choice of parameters for surface S_8 is $L_o = 3$, $M_o = 3$, $N_p/M_o = 5$.

The second point to note is that on any surface S_j, there is a similar optimal set of parameters $L_o = M_o$, $N_p/M_o = 5$ with, however, the critical L_o varying from surface to surface. Surfaces close to the measurement surface are characterized by higher values of L_o. This is a consequence of the fact that the effects of ill–posedness increase, not only with harmonic number, but also with distance from the measurement surface.

Finally, observe that the formulation of the Solution Procedure is such that the number of output harmonics can be varied from surface to surface. Therefore, in a maximally efficient experimental implementation, one chooses M_o from a surface relatively close to the measurement surface. For instance, on S_3 the saturation in accuracy occurs at $M_o = 6$. To resolve the highest harmonic we require $N_p/M_o = 5$. Therefore, $N_p = 30$ represents the optimal number of measurement probes. The value of L_o is chosen as $L_o = M_o = 6$ for surfaces close to the measurement surface S_1. As one moves inward, away from S_1, M remains fixed at $M = M_o = 6$ (there is no reason not to use every piece of available data) but the value of L_o is gradually decreased because of ill–posedness so that, on surfaces S_8 and S_9, $L_o = 3$. This simple procedure leads to the optimal choise of experimental parameters.

H Error Analysis

The fact that an optimal L_o exists is a result of the competition between ill-posedness in the formulation and poor resolution due to truncation. The former would require a small number of harmonics, since the highest ones diverge fastest, while the latter would require a large number of harmonics to maintain accuracy in the Fourier series representation. Indeed, the optimal L_o is expected and observed to be a function of the error level in the measurements as well as a function of the distance between the calculation and measurement surfaces.

A simple model based on the right circular cylinder of Section I demonstrates both of these effects as well as predicting the saturation of L_o with M for large M. Consider the problem

$$\nabla^2\phi = 0, \tag{116}$$

with boundary conditions

$$\phi(r=a) = \sum_{n=0}^{M}(\phi_n + \varepsilon_n)\cos n\theta, \tag{117}$$

$$\frac{\partial\phi}{\partial r}(r=a) = \frac{1}{a}\sum_{n=0}^{M} n(\phi_n - \varepsilon_n)\cos n\theta. \tag{118}$$

The analytic solution corresponding to these boundary conditions is given by

$$\phi(r,\theta) = \sum_{n=0}^{M}\left[\phi_n\left(\frac{r}{a}\right)^n + \varepsilon_n\left(\frac{a}{r}\right)^n\right]\cos n\theta. \tag{119}$$

The coefficients ϕ_n represent the "exact" answer, while the coefficients ε_n represent the "error" in the boundary data which renders the solution singular at the center of the cylinder. The correct solution with no errors that is regular at the origin, is of course, written as

$$\phi_R = \sum_{n=0}^{M}\phi_n\left(\frac{r}{a}\right)^n\cos n\theta. \tag{120}$$

Assume now, in analogy with the Solution Procedure, that the solution given by equation (119) is truncated using $L \leq M$ harmonics. This solution, denoted by ϕ_T, has the form

$$\phi_T = \sum_{n=0}^{L}\left[\phi_n\left(\frac{r}{a}\right)^n + \varepsilon_n\left(\frac{a}{r}\right)^n\right]\cos n\theta. \tag{121}$$

The difference between ϕ_T and ϕ_R is a measure of the error between the calculated and the exact solutions. Writing $\Delta\phi = \phi_T - \phi_R$ we obtain

$$\Delta\phi(r,\theta) = \sum_{n=0}^{L} \varepsilon_n \left(\frac{a}{r}\right)^n \cos n\theta - \sum_{L+1}^{M} \phi_n \left(\frac{r}{a}\right)^n \cos n\theta. \tag{122}$$

Note that the last term in equation (122) is non–zero for $L \leq M-1$ and vanishes for $L = M$. Defining the RMS error as usual by

$$< \varepsilon^2(r) >= \left[\frac{1}{2\pi}\int_0^{2\pi} d\theta\,(\Delta\phi)^2\right] \Big/ \phi_M^2, \tag{123}$$

where $\phi_M = \max_\theta |\phi(a,\theta)|$, yields

$$2 < \varepsilon^2 >= \sum_{n=0}^{L} \left(\frac{\varepsilon_n}{\phi_M}\right)^2 \left(\frac{a}{r}\right)^{2n} + \sum_{L+1}^{M} \left(\frac{\phi_n}{\phi_M}\right)^2 \left(\frac{r}{a}\right)^{2n}. \tag{124}$$

Equation (124) can be qualitatively generalized to non–circular cross–sections by replacing r^2/a^2 by $x_j = A_j/A_1$, the ratio of the cross–sectional areas of the calculation and measurement surfaces. The first term in equation (124) represents the errors due to ill–posedness while the second term represents the errors resulting from the truncation of the Fourier series.

To proceed further we need knowledge of the n-dependences of ε_n and ϕ_n. As a simple model that is also quite realistic in comparison with the experimental situation we assume

$$\frac{\varepsilon_n}{\phi_M} = \frac{\varepsilon_M}{\sqrt{3}}, \tag{125}$$

$$\frac{\phi_n}{\phi_M} = Ae^{-\alpha n}. \tag{126}$$

Equation (125) indicates that the error in the data is independent of n, and the standard deviation of a uniform random distribution has been used to denote the magnitude of the error. In practice, typical experimental errors in the measurements lead to a slowly decreasing dependence of ε_n on n. Assuming that the errors in the measurements are random, we have

$$\varepsilon_n = \frac{1}{2\pi}\int_0^{2\pi} \phi(a,\theta)\varepsilon_M r_i \cos n\theta d\theta, \tag{127}$$

where r_i is a random number in the interval $[-1, 1]$. Since $\phi\varepsilon_M r_i$ is of bounded variation, we can use Riemann's Lemma[11] to estimate the magnitude of ε_n:

$$\varepsilon_n \sim \frac{\phi_M \varepsilon_m r_i}{n}. \tag{128}$$

Taking the standard deviation of a uniform random distribution as a measure of the magnitude of r_i, we finally obtain

$$\frac{\varepsilon_n}{\phi_M} \sim \frac{\varepsilon_M}{\sqrt{3}n}. \tag{129}$$

However, the exponential dependence associated with $(a/r)^{2n}$ dominates the behaviour so that treating ε_n as a constant is a reasonable approximation and greatly simplifies the analysis.

The assumption $\phi_n/\phi_M = Ae^{-\alpha n}$ is an accurate approximation to typical Alcator C-MOD data using an elliptically shaped measurement surface. For the test case the parameter $\alpha \simeq 0.5$, and the amplitude $A \simeq 1$. Under more general conditions, one still expects ϕ_n to be a rapidly decreasing function of n for large n, and the choice of an exponential decay with a free fitting parameter α leads to a considerable simplification of the analysis.

Equations (125) and (126) are substituted into equation (124) and the summations carried out. The result is

$$2 < \varepsilon^2 >= \frac{\varepsilon_M^2}{3x_j^L}\left[\frac{1 - x_j^{L+1}}{1 - x_j}\right] + A^2(\lambda x_j)^{L+1}\left[\frac{1 - (\lambda x_j)^{M-L}}{1 - \lambda x_j}\right], \tag{130}$$

where $\lambda = e^{-2\alpha}$. The RMS error $< \varepsilon^2 >^{1/2}$ is sketched in Figure 17a. Note that there are two possibilities. In case (a) the error has a minimum for a value $L_o < M$. A straightforward calculation yields

$$L_o = \ln\left[\frac{\varepsilon_M^2}{3A^2}\frac{(1 - \lambda x_j)\ln x_j}{(1 - x_j)\lambda x_j \ln \lambda x_j}\right] \Big/ \ln(\lambda x_j^2). \tag{131}$$

For case (b) the minimum in $< \varepsilon^2 >$ occurs for a value $L > M$, violating the condition for validity $L \leq M$. In this case, the minimum allowable value of $< \varepsilon^2 >$ occurs on the boundary and

$$L_o = M. \tag{132}$$

A plot of L_o versus M is illustrated in Figure 17b. Observe the similarities between Figures 17b and 16. The transition value of M is given by $M_o = L_o$, defined by equation (131). The optimal experimental design for a given surface corresponds to $L = M = L_o$ and $N_p/M = 5$. This leads to the minimum error with the fewest number of probes. A comparison between the observed L_o and that calculated using equation (131) is given for $\alpha = 0.5$, $\varepsilon_M = 0.01$ in Table 1. The agreement is seen to be good for a large range of values of x_j. The variation of L_o with ε_M is illustated in Table 2 for the case $x_j = 0.441$, $\alpha = 0.5$. As expected, larger ε_M require smaller values of L to minimize the effects of ill–posedness. The simple model thus explains all the qualitative features obtained from the full numerical studies.

V Conclusion

We have formulated a Green's function method for reconstructing the poloidal flux surfaces in the vacuum region of a tokamak based on magnetic measurements on a boundary surface at the vacuum vessel wall. The method is very fast to use in a practical situation, and the accuracy is comparable to the accuracy of the input data. We have also addressed the issue of the number of probes required for sufficiently accurate input data, and based on our analysis can conclude that in most cases no more than 30 probes are necessary.

VI Acknowledgments

We are indebted to Prof. Ian Hutchinson for useful discussions and suggestions throughout the course of this work and are grateful to Dr. Bas Braams of Princeton Plasma Physics Laboratory for many valuable comments. We also thank Vonya Perham for helping us type parts of the manuscript and Gerasimos Tinios for writing a substantial portion of the computer code.

VII References

[1] Shafranov, V. D., Sov. Phys.–JETP **26** (1960), 682.

[2] Marchuk, G. I., "Methods of Numerical Mathematics", 2nd ed., Springer, New York, 1982.

[3] Bondarenko, S. P., V. E. Golant, M. P. Gryaznevich, Yu. K. Kuznetsov, V. N. Pyatov, *et.al.* Soviet J. Plasma Phys. **10** (1984), 520.

[4] Lee, D. K. and Y.-K. M. Peng, J. Plasma Phys. **25** (1981), 161.

[5] Wootton, A. J., Nucl. Fus. **19** (1979), 987.

[6] Swain, D. W. and G. H. Nielson, Nucl. Fus. **22** (1982), 1015.

[7] Lao, L. L., H. St. John, R. D. Stambaugh, A. G. Kellman and W. Pfeiffer, Nucl. Fus. **25** (1985), 1611.

[8] Feneberg, W., K. Lackner and P. Martin, Comput. Phys. Commun. **31** (1984), 143.

[9] Braams, B. J., *Report IPP 5/2, Max-Planck-Institut für Plasmaphysik, 1985.*

[10] Stratton, J. A., "Electromagnetic theory", McGraw–Hill, New York, 1941.

[11] Jeffreys, Sir H. and B. S. Jeffreys, "Methods of Mathematical Physics", 3rd ed., Cambridge University Press, Cambridge, 1978.

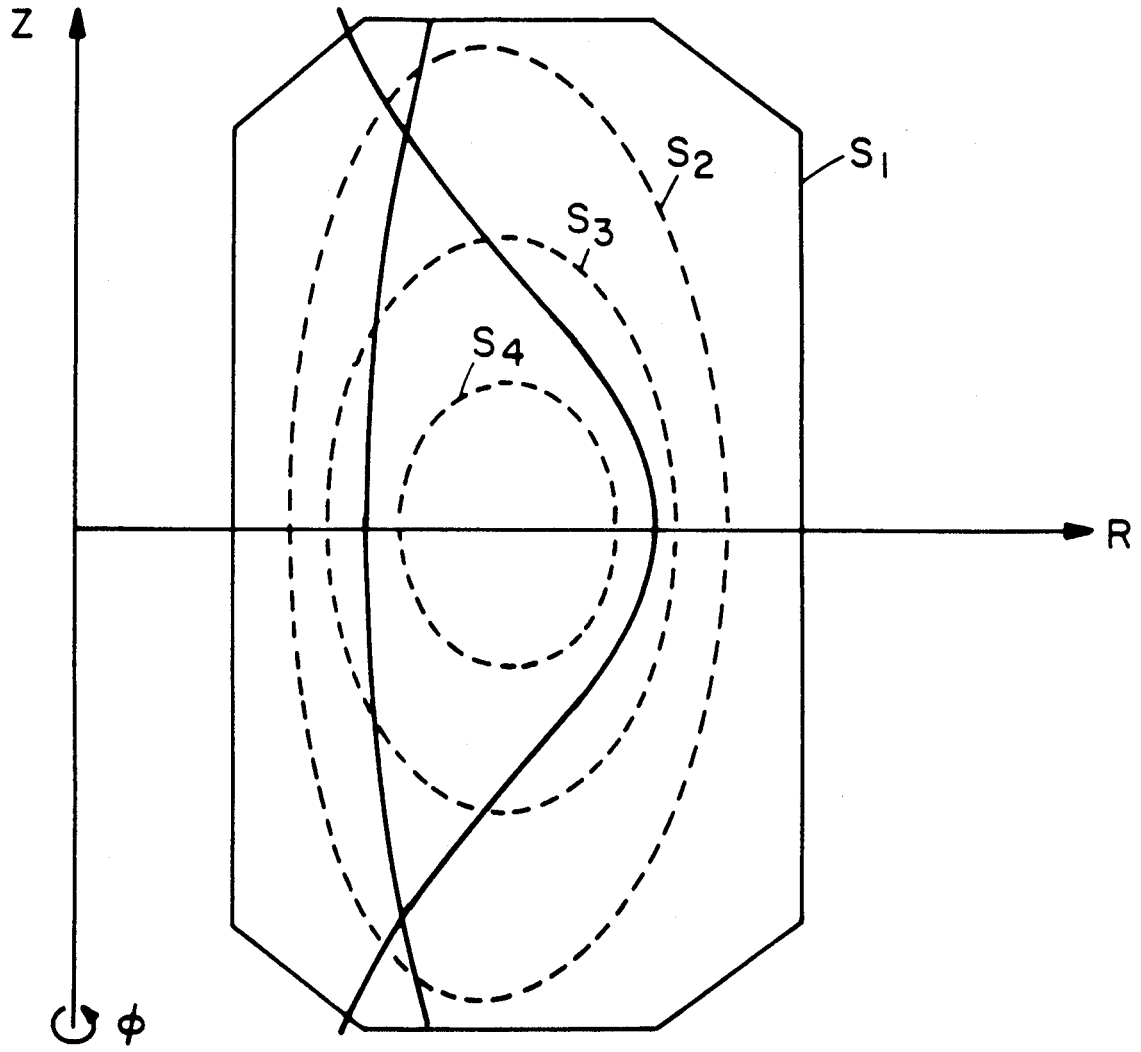

Figure 1 A typical experimental geometry.

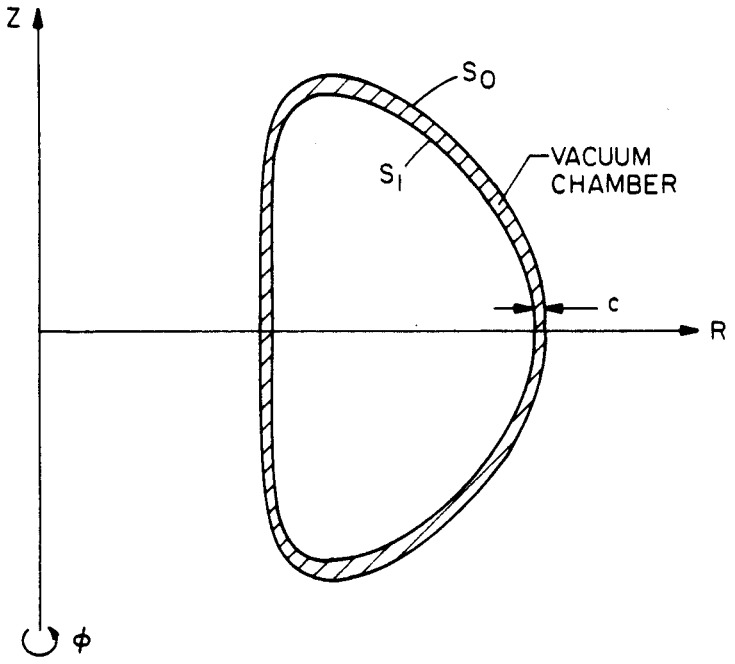

Figure 2a Vacuum chamber has finite thickness, c.

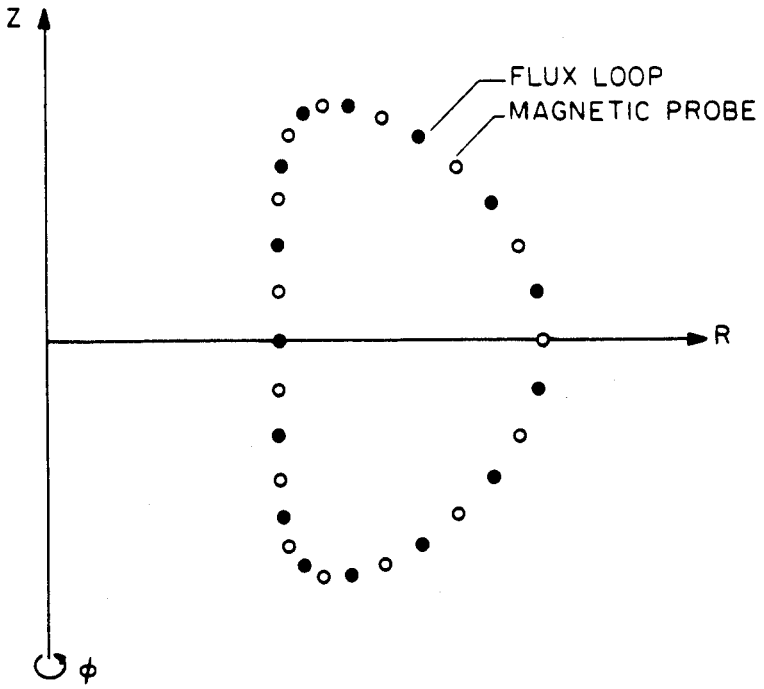

Figure 2b Flux probes (•) and field probes (○) do not coincide.

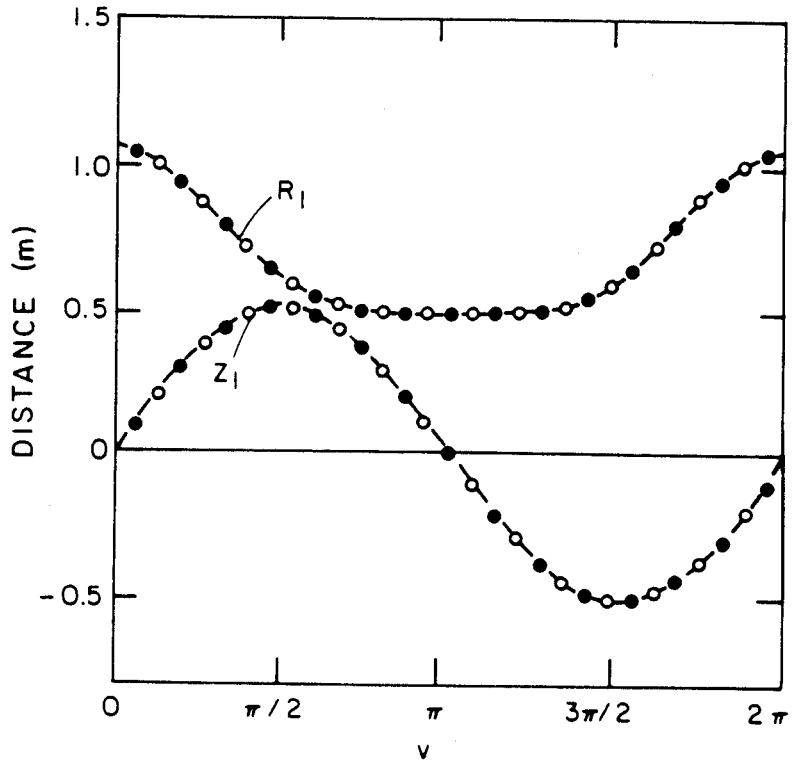

Figure 3a R and Z as functions of v. Bullets (•) denote flux probes and open circles (○) field probes.

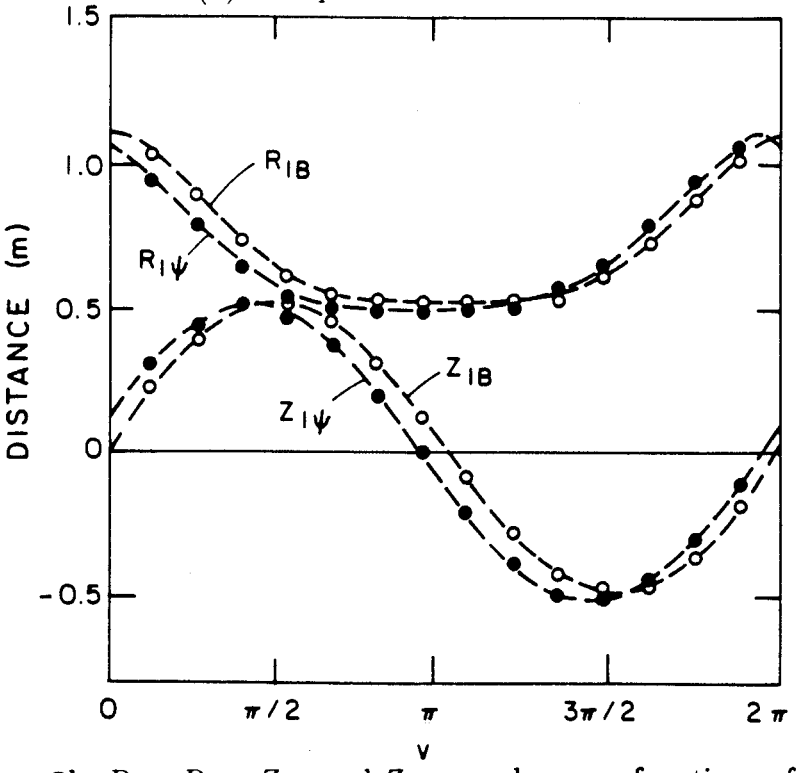

Figure 3b $R_{1\psi}$, R_{1B}, $Z_{1\psi}$ and Z_{1B} are shown as functions of v.

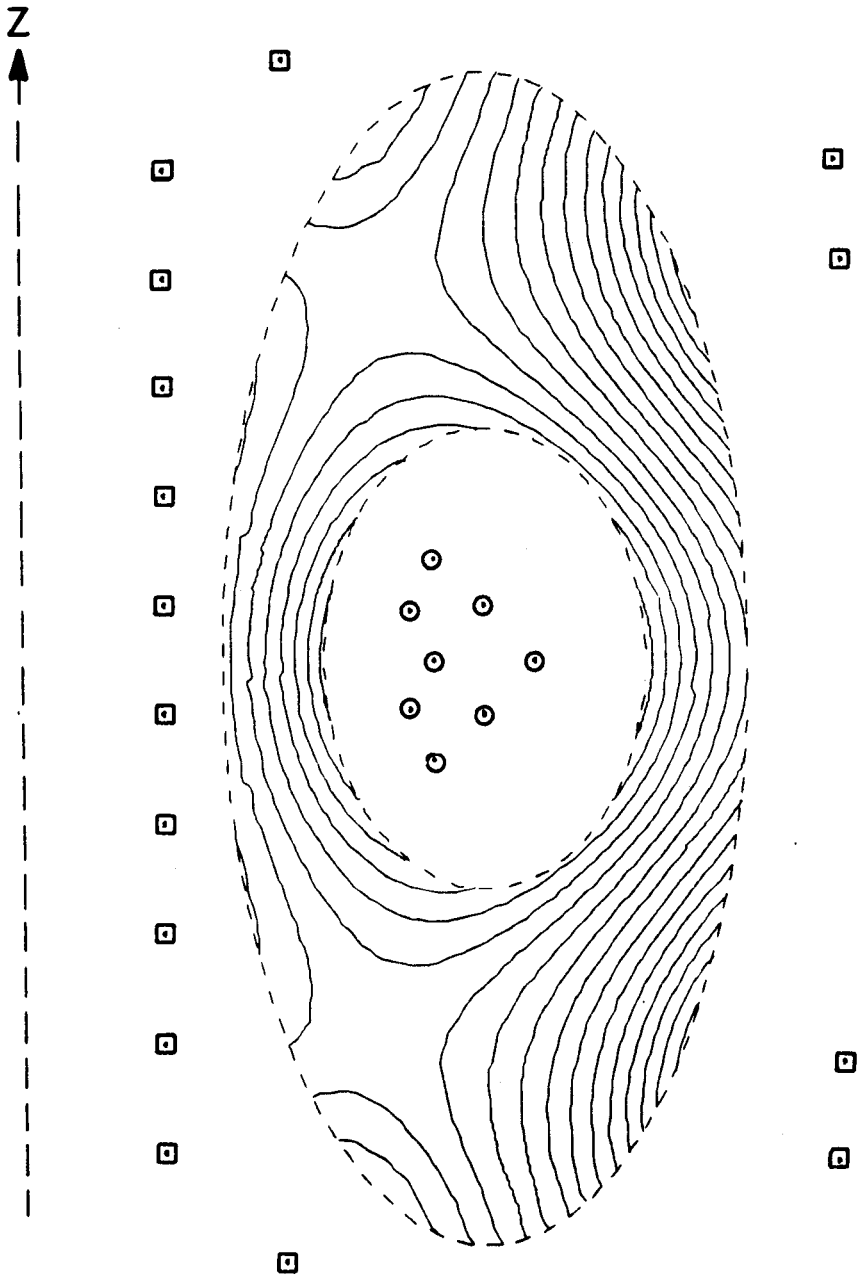

Figure 4 The analytic flux countours of our Test Case.

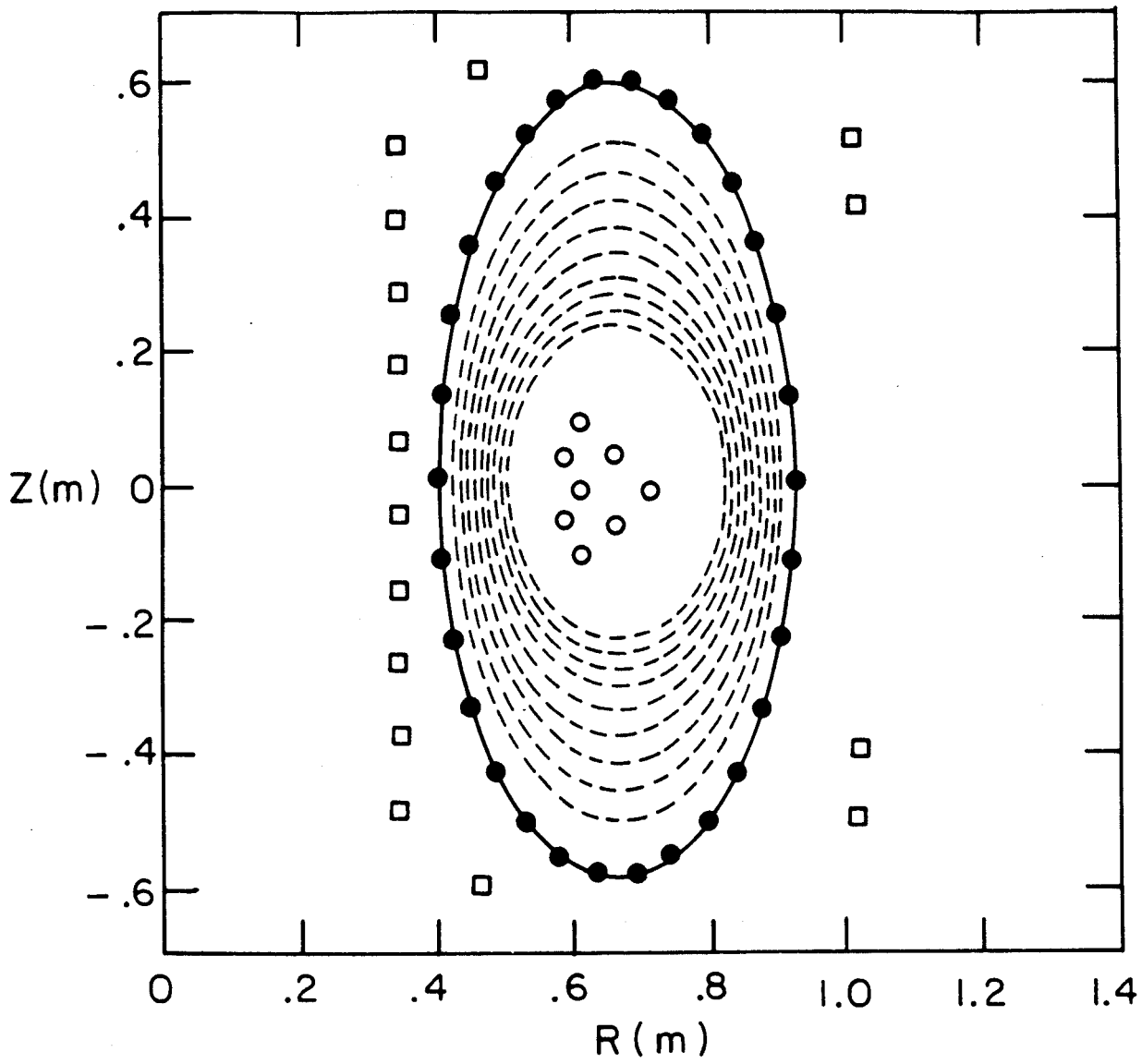

Figure 5 Calculation geometry. Also shown are external coils (□), probe locations (•) and filaments representing plasma (○).

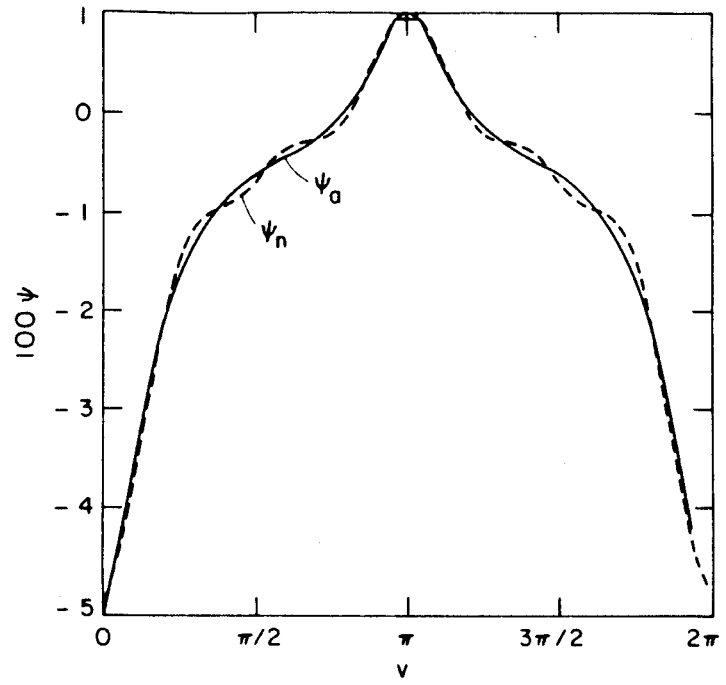

Figure 6a ψ_a (solid) and ψ_n (dashed) along measurement boundary.

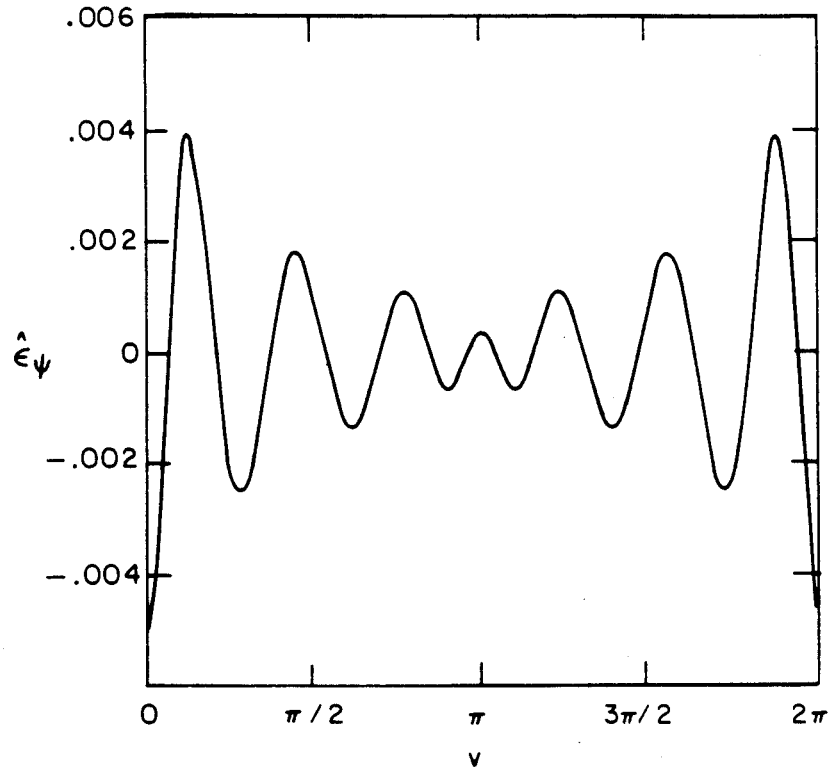

Figure 6b $\hat{\epsilon}_\psi$ along measurement boundary.

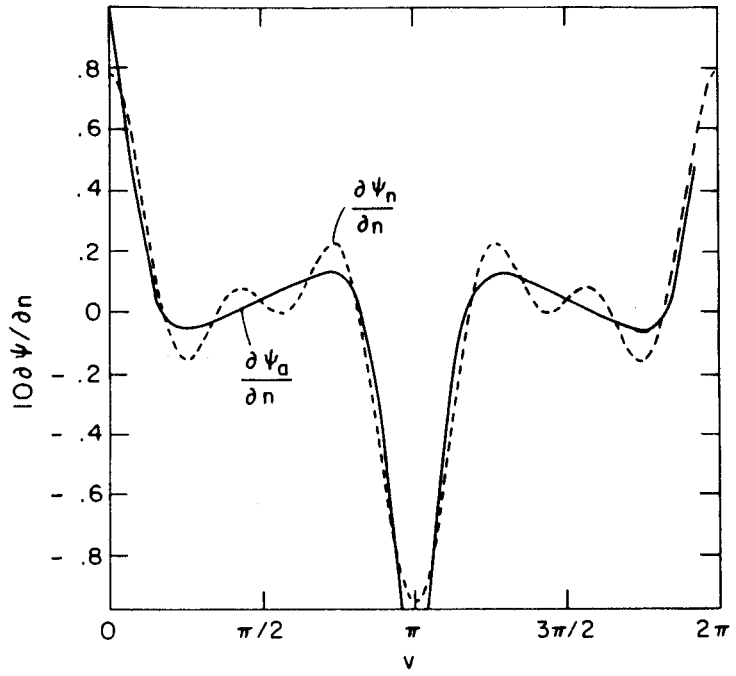

Figure 6c $\partial\psi_a/\partial n$ (solid) and $\partial\psi_n/\partial n$ (dashed) along measurement boundary.

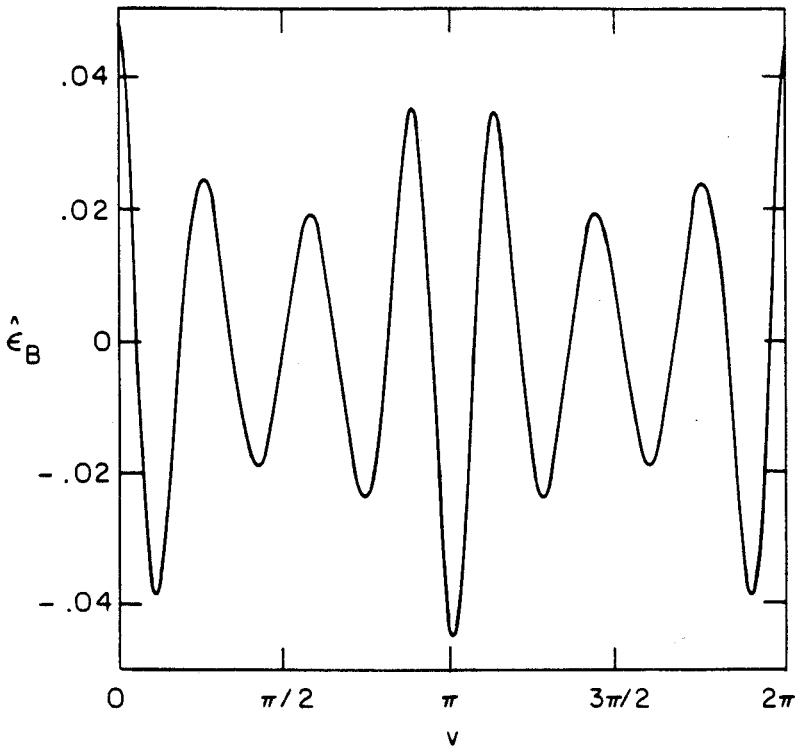

Figure 6d $\hat{\epsilon}_B$ along measurement boundary.

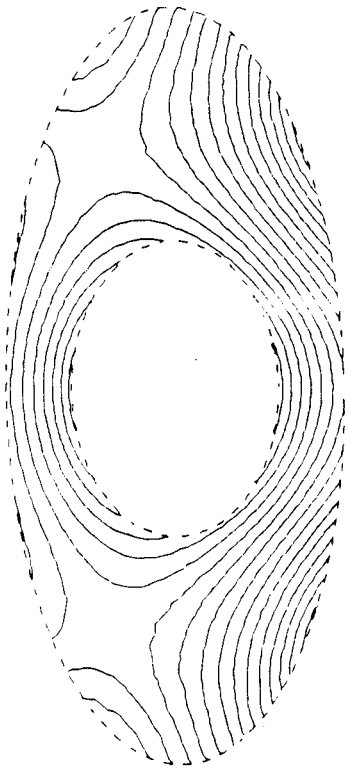

Figure 7a Calculated flux contours — external currents subtracted.

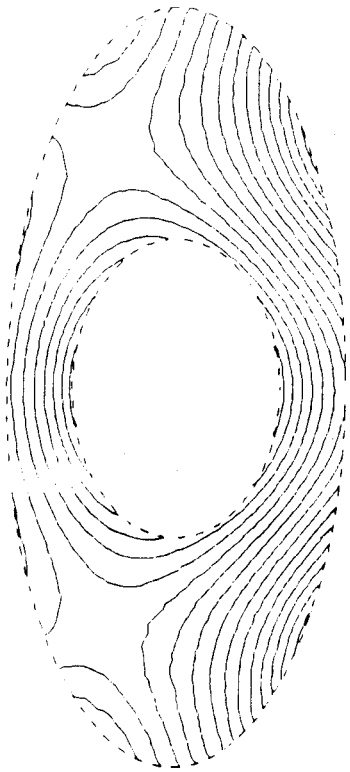

Figure 7b Corresponding analytic flux contours.

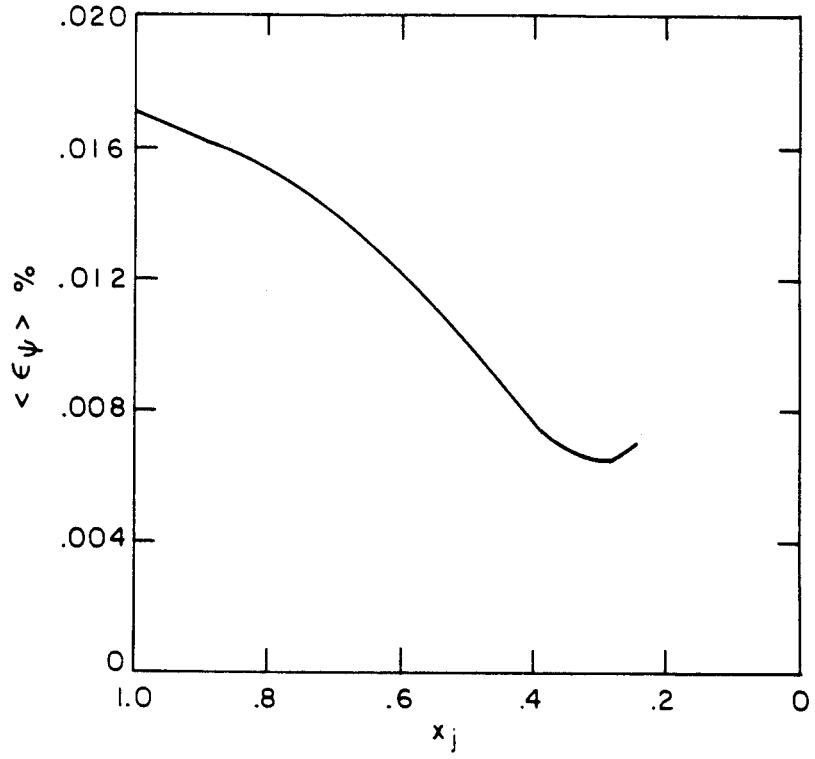

Figure 8a $< \epsilon_\psi >$ as function of x_j.

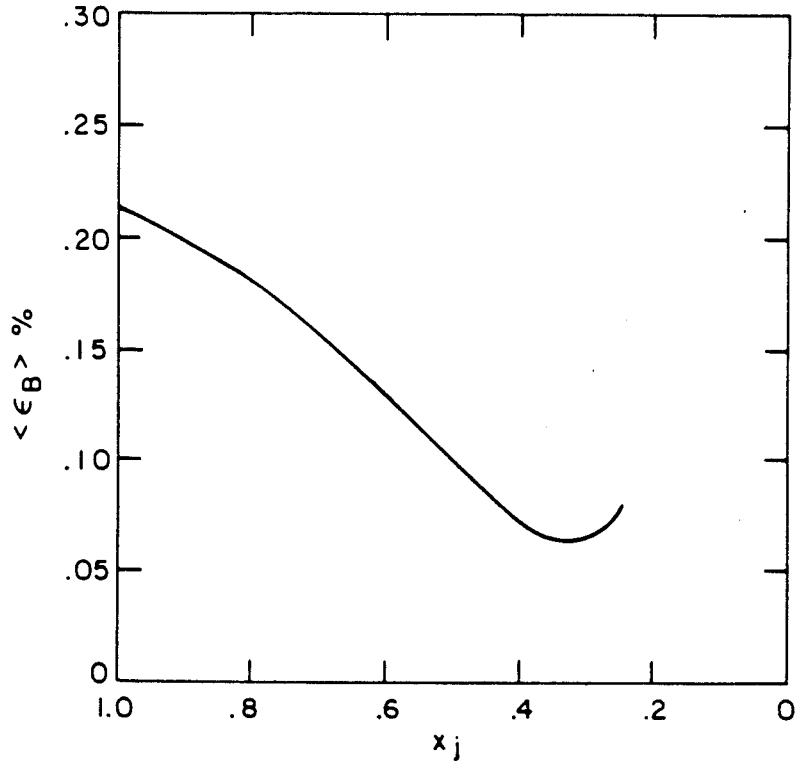

Figure 8b $< \epsilon_B >$ as function of x_j.

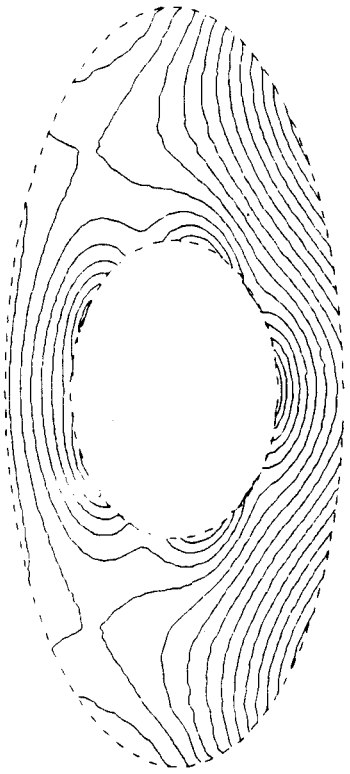

Figure 9a Calculated flux contours — external currents kept in calculation.

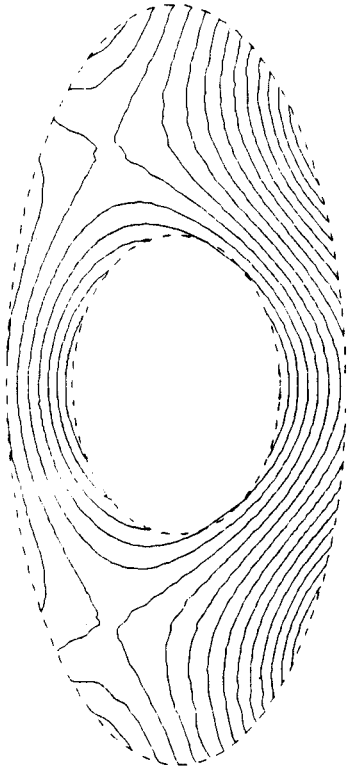

Figure 9b Corresponding analytic flux countours.

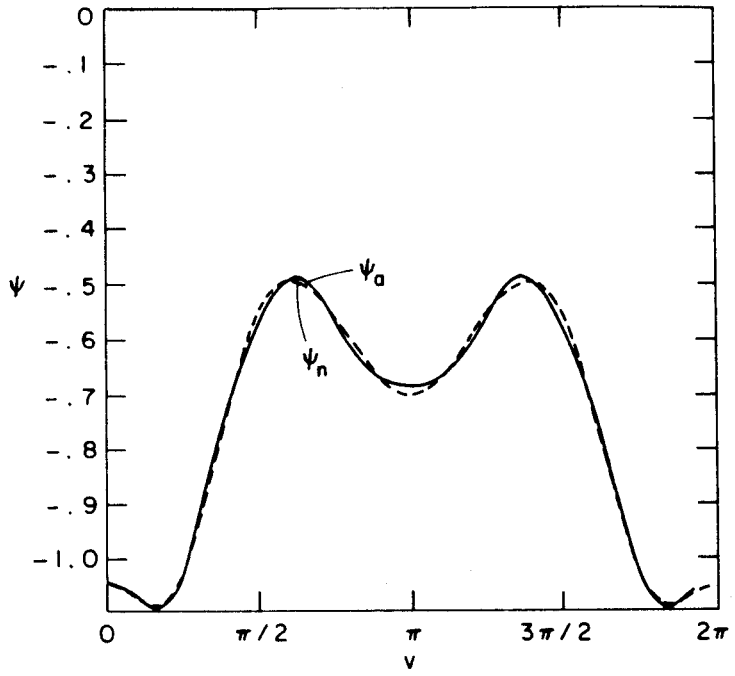

Figure 10a ψ_a (solid) and ψ_n (dashed) along S_1 when external currents are kept in calculation.

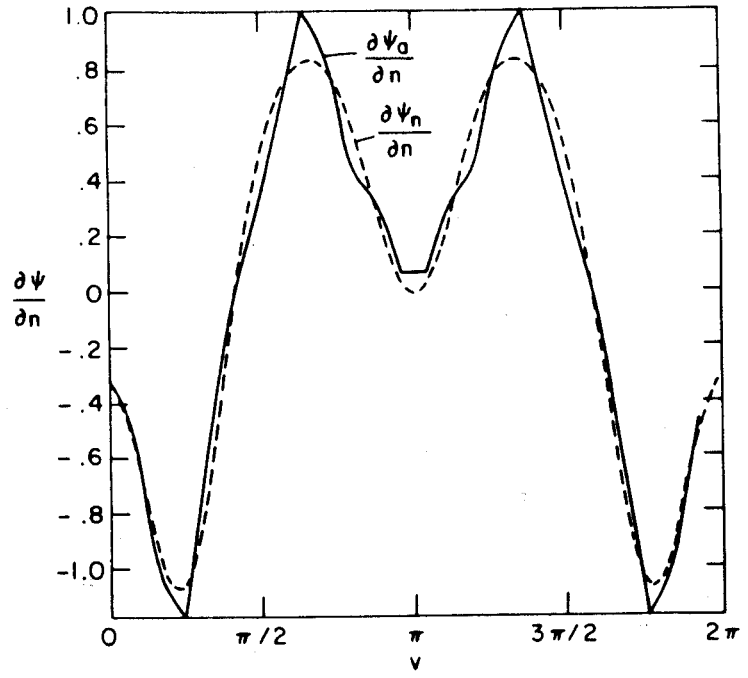

Figure 10b $\partial\psi_a/\partial n$ (solid) and $\partial\psi_n/\partial n$ (dashed) along S_1 for the same case.

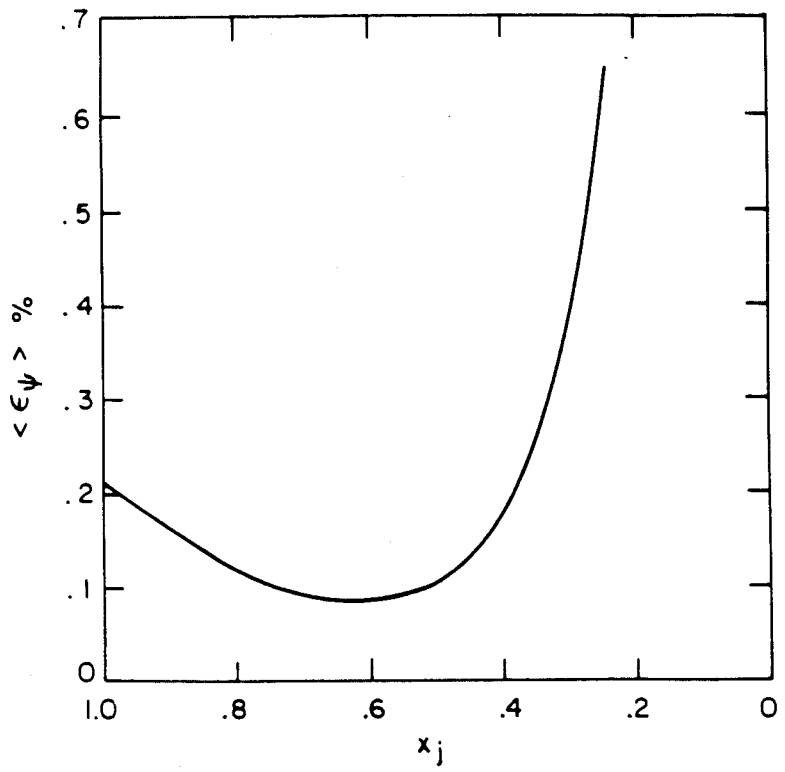

Figure 11a $< \epsilon_\psi >$ as function of x_j when external currents are kept in calculation.

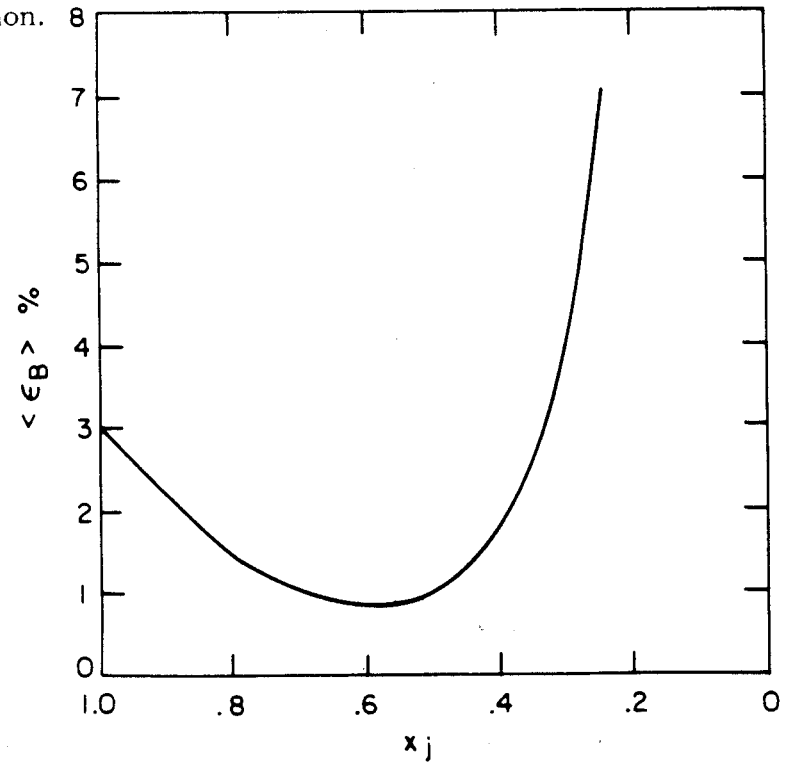

Figure 11b $< \epsilon_B >$ as function of x_j for the same case.

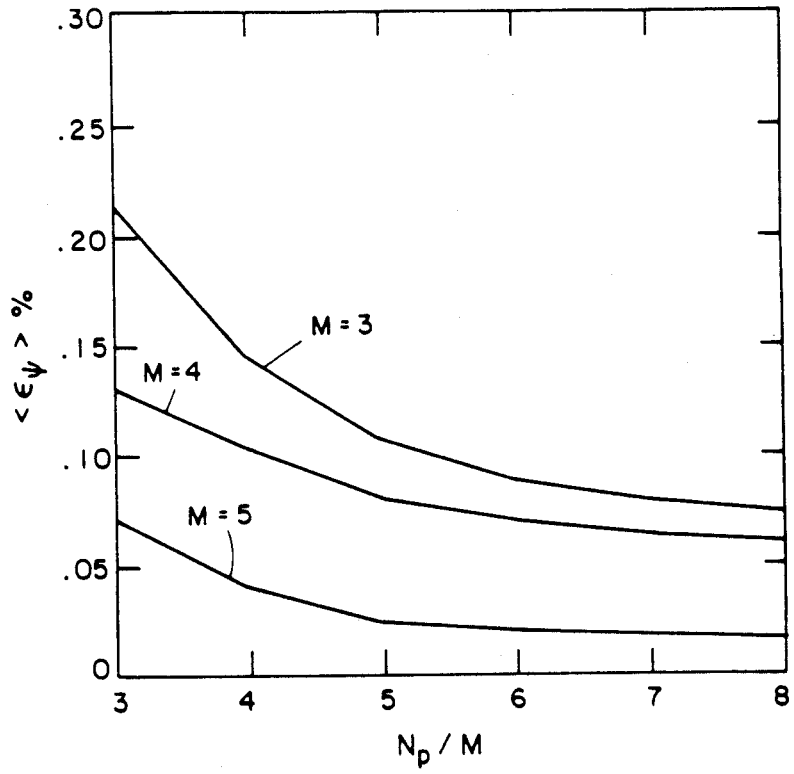

Figure 12a $< \epsilon_\psi >$ as function of N_p/M for $M = 3, 4, 5$ (from top to bottom).

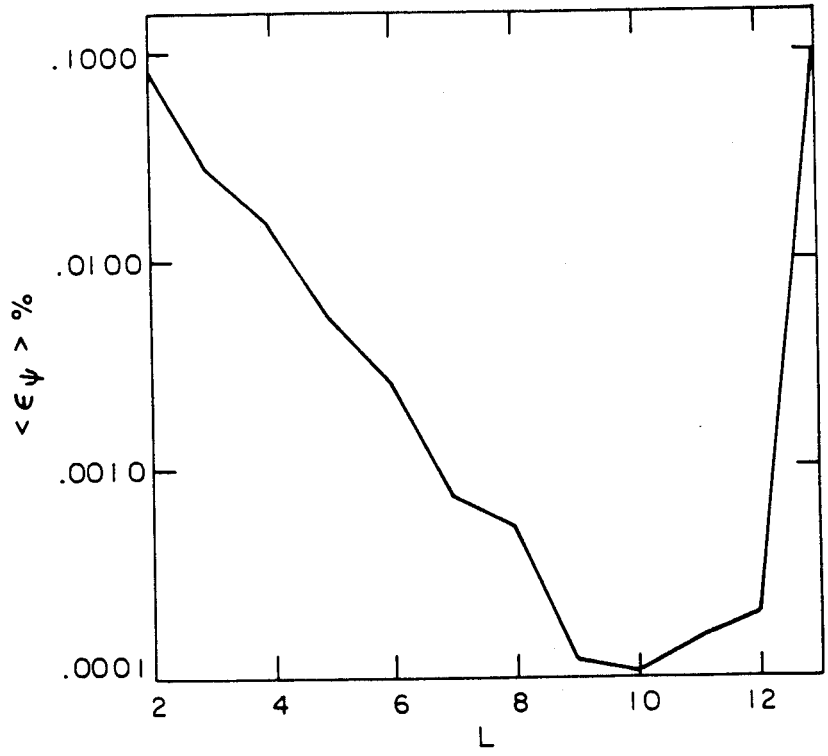

Figure 12b $< \epsilon_\psi >$ as a function of output harmonics L for surface S_8.

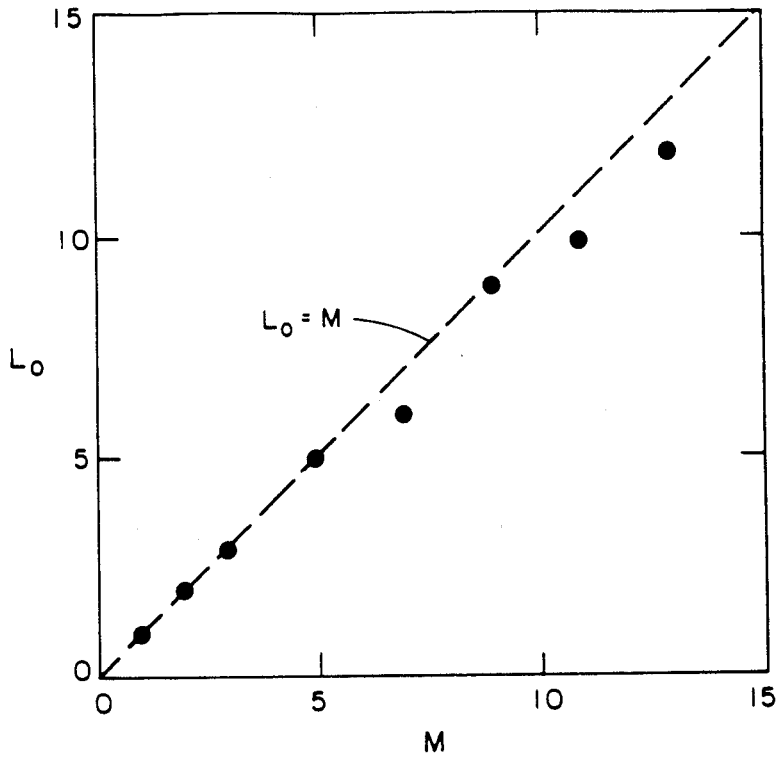

Figure 13a L_o as function of M for surface S_4, $\varepsilon_M = 0$.

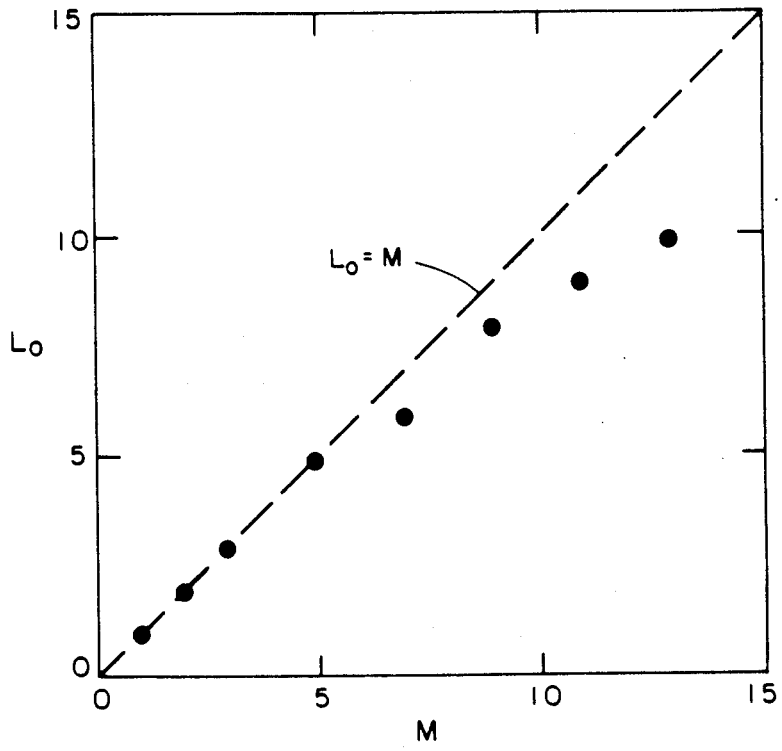

Figure 13b L_o as function of M for surface S_8, $\varepsilon_M = 0$.

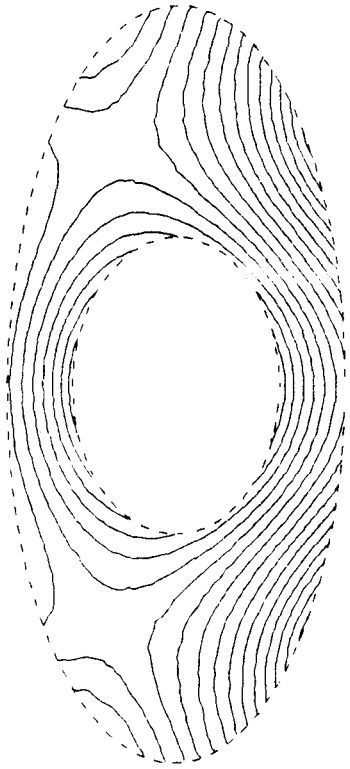

Figure 14a Calculated flux contours, $\varepsilon_M = 1\%$.

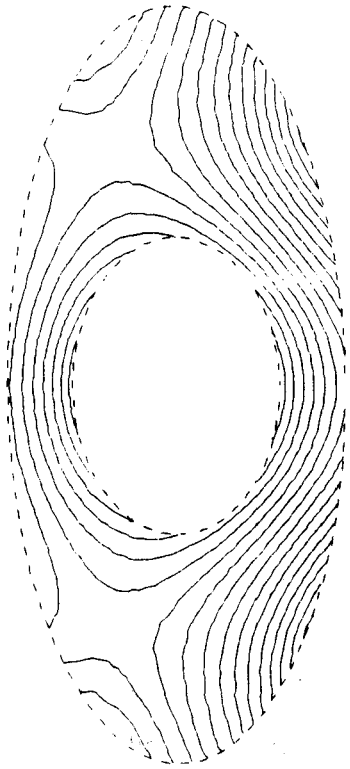

Figure 14b Corresponding analytic flux contours.

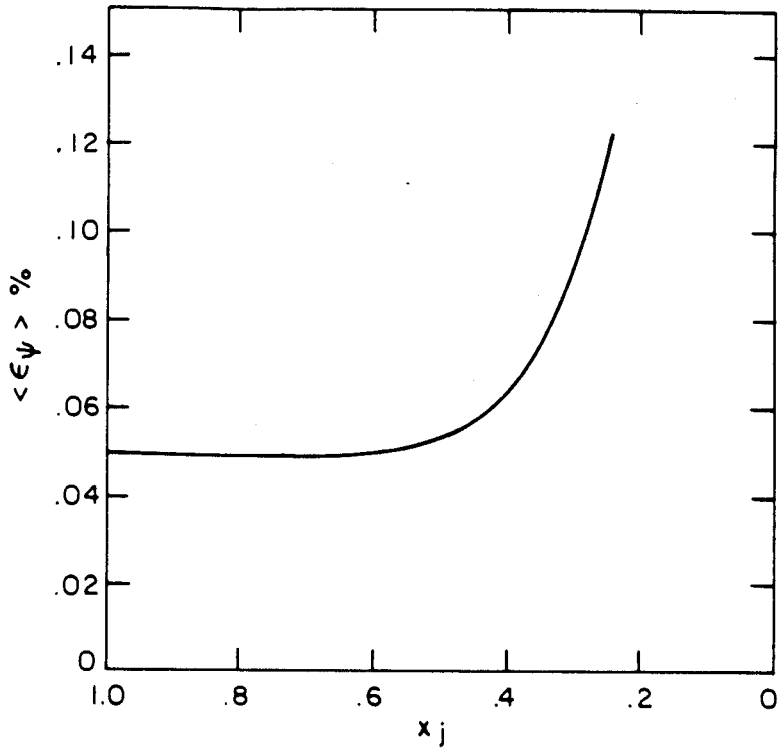

Figure 15a $< \epsilon_\psi >$ as function of x_j, $\epsilon_M = 1\%$.

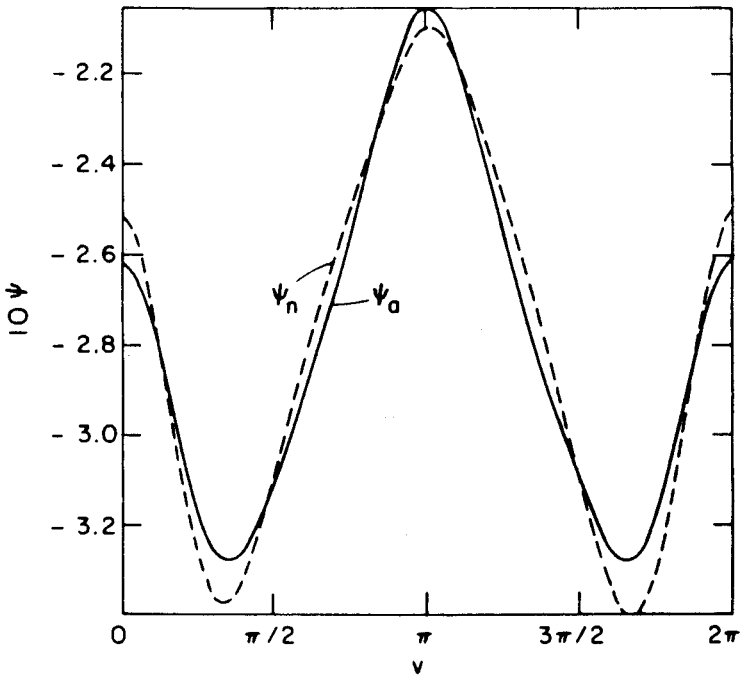

Figure 15b ψ_a (solid) and ψ_n (dashed) for surface S_9.

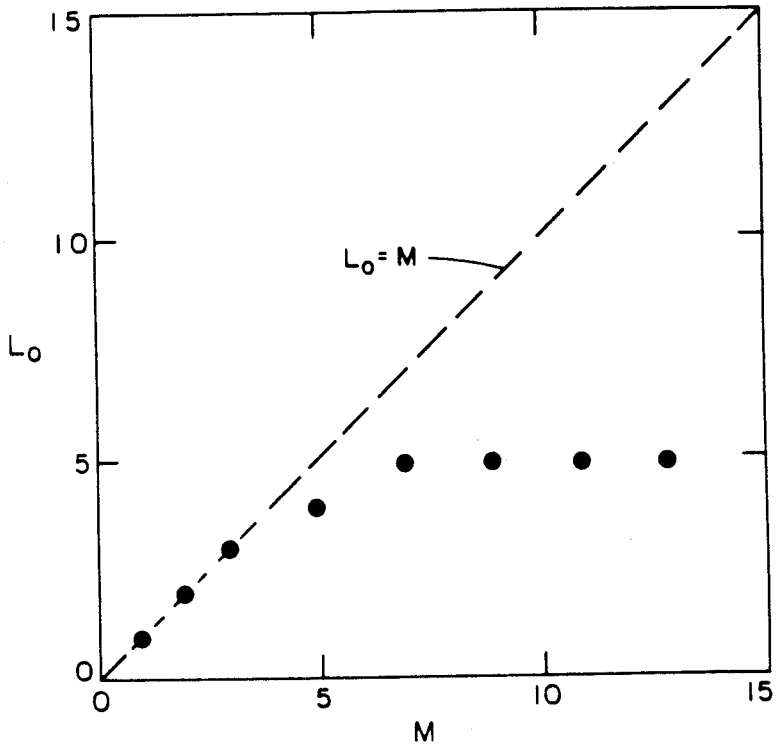

Figure 16a L_o as function of M for surface S_4, $\varepsilon_M = 1\%$.

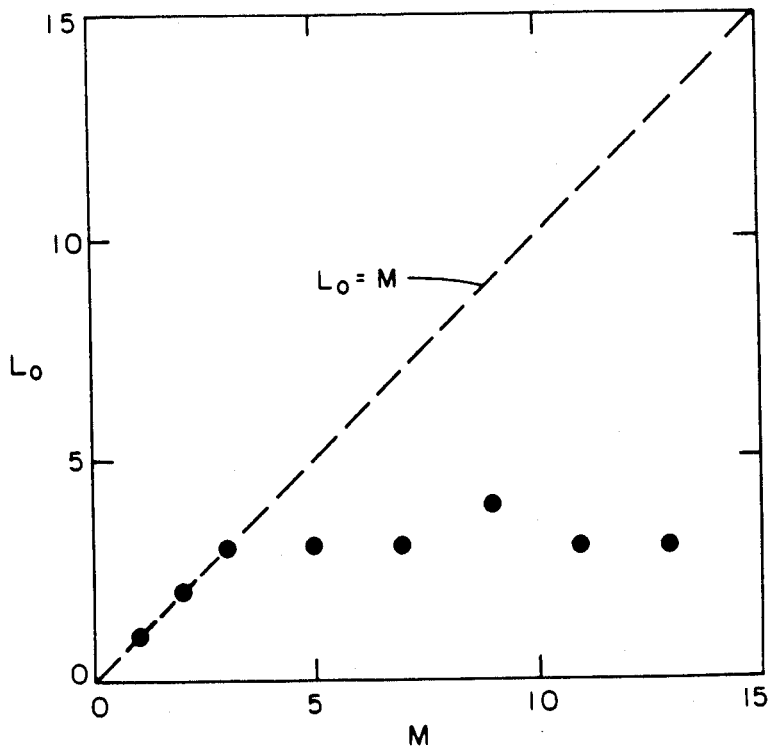

Figure 16b L_o as function of M for surface S_8, $\varepsilon_M = 1\%$.

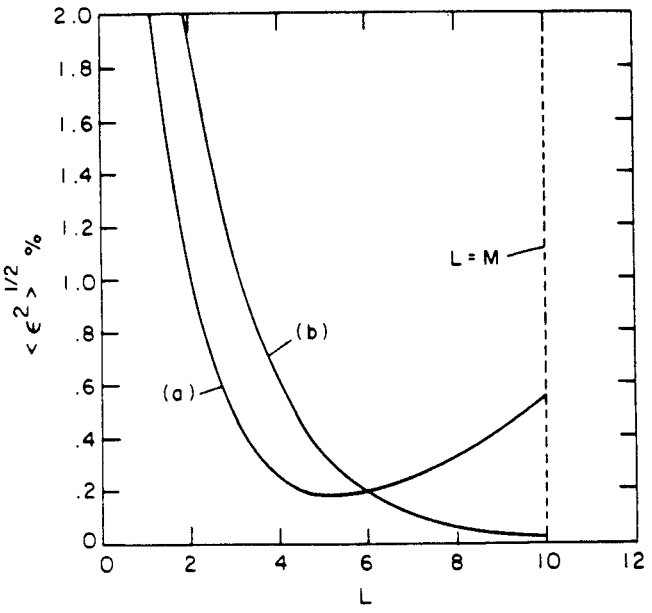

Figure 17a The RMS error $< \epsilon^2 >^{1/2}$ as a function of output harmonics L with $\epsilon_M = 1\%$.

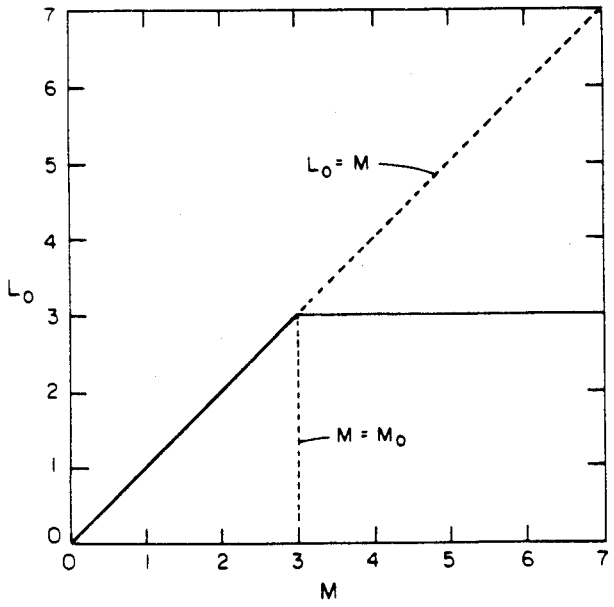

Figure 17b The optimal number of output harmonics L_o versus the number of input harmonics M for $x_j = 0.591$ with $\epsilon_M = 1\%$.

x_j	Expected L_o	Observed L_o
0.241	2	3
0.283	2	3
0.326	3	4
0.375	3	5
0.441	3	5
0.515	4	6
0.591	5	6
0.686	5	7
0.784	6	7

Table 1 The optimal L_o as calculated from equation (131) (expected L_o) and the corresponding observed L_o for $\varepsilon_M = 1\%$ are shown for each calculation surface.

ε_M %	Expected L_o	Observed L_o
0.5	4	5
1.0	3	5
1.5	3	3
2.0	3	3
3.0	3	3
5.0	2	3

Table 2 The optimal L_o as calculated from equation (131) (expected L_o) and the corresponding observed L_o for $x_j = 0.441$ are shown for some values of ε_M.

Appendix A Vector Green's Theorem

This section contains a derivation of the Vector Green's Theorem, a related but less well known form of the usual Green's Theorem. This theorem is used for determining the interior flux surfaces, and its specific application is given in section III.

The derivation begins with the vector identity

$$\nabla \cdot (\mathbf{A} \times \nabla \times \mathbf{G} - \mathbf{G} \times \nabla \times \mathbf{A}) = \mathbf{G} \cdot \nabla \times \nabla \times \mathbf{A} - \mathbf{A} \cdot \nabla \times \nabla \times \mathbf{G}. \tag{A1}$$

Assume that $\mathbf{A}$ is the vector potential and the region of interest corresponds to a pure vacuum; for instance the region between the vacuum chamber and the last plasma flux surface to carry current. In such a region $\mathbf{A}$ satisfies

$$\nabla \times \nabla \times \mathbf{A} = 0. \tag{A2}$$

Assume that $\mathbf{G}$ is chosen as follows:

$$\mathbf{G} = \frac{\mathbf{C}}{r}, \tag{A3}$$

where

$$r = \left[(x' - x)^2 + (y' - y)^2 + (z' - z)^2 \right]^{1/2}, \tag{A4}$$

and

$$\mathbf{C} = C_1 \mathbf{e}_x + C_2 \mathbf{e}_y + C_3 \mathbf{e}_z \tag{A5}$$

is an arbitrary constant vector.

One now integrates over some vacuum region and uses the divergence theorem. The result is

$$\int \mathbf{A}' \cdot \nabla' \times \nabla' \times \mathbf{G}\, d\mathbf{x}' = -\sum_j{}' \int \mathbf{n}' \cdot (\mathbf{A}' \times \nabla' \times \mathbf{G} - \mathbf{G} \times \nabla' \times \mathbf{A}')\, dS_j'. \tag{A6}$$

In Eq. (A6) prime denotes the integration variable and the unprimed quantities in $\mathbf{G}$ denote the observation point. The notation $\sum'$ denotes the fact that the observation point (x, y, z) is excluded from the domain of integration and is surrounded by a sphere (or hemisphere) if it lies inside (or on) the vacuum region. A contribution from the surface of this sphere (or hemisphere) is included in the right hand side.

The next step is to simplify the individual terms appearing in Eq. (A6). The following relations are helpful in this connection. First, since $\mathbf{C}$ is a constant vector

$$\nabla \times \mathbf{G} = -\mathbf{C} \times \nabla \frac{1}{r}. \tag{A7}$$

Second, since $\nabla^2(1/r) = 0$ for $r \neq 0$

$$\nabla \times \nabla \times \mathbf{G} = \nabla \left(\mathbf{C} \cdot \nabla \frac{1}{r} \right). \tag{A8}$$

Using Eq. (A7) one can easily show that

$$\mathbf{n} \cdot \mathbf{A} \times \nabla \times \mathbf{G} = \mathbf{C} \cdot (\mathbf{n} \times \mathbf{A}) \times \nabla \frac{1}{r}, \tag{A9}$$

$$\mathbf{n} \cdot \mathbf{G} \times \nabla \times \mathbf{A} = -\frac{\mathbf{C} \cdot \mathbf{n} \times \nabla \times \mathbf{A}}{r}. \tag{A10}$$

If one now uses the gauge condition $\nabla \cdot \mathbf{A} = 0$ then Eq. (A6) can be rewritten as

$$\mathbf{C} \cdot \sum_j{}' \int \left[(\mathbf{n}' \cdot \mathbf{A}') \nabla' \frac{1}{r} + (\mathbf{n}' \times \mathbf{A}') \times \nabla' \frac{1}{r} + \frac{\mathbf{n}' \times \nabla' \times \mathbf{A}'}{r} \right] dS_j' = 0. \tag{A11}$$

Since $\mathbf{C}$ is an arbitrary vector,

$$\sum_{j=1}^{3}{}' \int \left[(\mathbf{n}' \cdot \mathbf{A}') \nabla' \frac{1}{r} + (\mathbf{n}' \times \mathbf{A}') \times \nabla' \frac{1}{r} + \frac{\mathbf{n}' \times \nabla' \times \mathbf{A}'}{r} \right] dS_j' = 0. \tag{A12}$$

The last step in the derivation is to evaluate the contribution over the observation point analytically in the limit where the sphere (or hemisphere) surrounding it shrinks to zero. In a small sphere (or hemisphere) surrounding the observation point

$$\nabla \frac{1}{r} = -\frac{\mathbf{e}_r}{r^2},$$

$$\mathbf{n} = -\mathbf{e}_r. \tag{A13}$$

The contribution to Eq. (A12) from the observation point is given by

$$I_o \equiv \int \left[\left(\frac{\mathbf{e}_r \cdot \mathbf{A}'}{r^2} \right) \mathbf{e}_r + \frac{(\mathbf{e}_r \times \mathbf{A}') \times \mathbf{e}_r}{r^2} - \frac{\mathbf{e}_r \times \nabla' \times \mathbf{A}'}{r} \right] dS'_o, \tag{A14}$$

and I_o is easily evaluated by noting that

$$\mathbf{e}_r \times (\mathbf{e}_r \times \mathbf{A}') = (\mathbf{e}_r \cdot \mathbf{A}')\,\mathbf{e}_r - \mathbf{A}', \tag{A15}$$

and that in the limit $r \to 0$

$$\int \mathbf{Q}\, dS'_o = \lim_{r \to 0} \left(\sigma 4\pi r^2 \mathbf{Q} \right). \tag{A16}$$

This allows us to write the Vector Green's Theorem in the form

$$\sigma \mathbf{A}(\mathbf{x}) = -\frac{1}{4\pi} \sum_j \int \left[(\mathbf{n}' \cdot \mathbf{A}')\, \nabla' \frac{1}{r} + (\mathbf{n}' \times \mathbf{A}') \times \nabla' \frac{1}{r} + \frac{\mathbf{n}' \times \nabla' \times \mathbf{A}'}{r} \right] dS'_j. \tag{A17}$$

In equations (A16) and (A17)

$$\sigma = \begin{cases} 1 & \text{interior observation point,} \\ 1/2 & \text{surface observation point,} \\ 0 & \text{exterior observation point,} \end{cases} \tag{A18}$$

and $\sum_j$ denotes summation over only the boundary surfaces.